

The 2-Higgs-Doublet Model with Soft CP-violation Confronting Electric Dipole Moments and Colliders

Kingman Cheung,^{a,b,c} Adil Jueid,^c Ying-nan Mao,^a Stefano Moretti^d

^a*Physics Division, National Center for Theoretical Sciences, Hsinchu, Taiwan 300*

^b*Department of Physics, National Tsing Hua University, Hsinchu, Taiwan 300*

^c*Division of Quantum Phases and Devices, School of Physics, Konkuk University, Seoul 143-701, Republic of Korea*

^d*School of Physics and Astronomy, University of Southampton, Southampton, SO17 1BJ, United Kingdom*

E-mail: cheung@phys.nthu.edu.tw, adiljueid@konkuk.ac.kr,
ynmao@cts.nthu.edu.tw, s.moretti@soton.ac.uk

ABSTRACT: We analyze CP-violating effects in both Electric Dipole Moment (EDM) measurements and future analyses at the Large Hadron Collider (LHC) assuming a 2-Higgs-Doublet Model (2HDM) with “soft” CP-violation. Our analysis of EDMs and current LHC constraints shows that, in the case of a 2HDM Type II and Type III, an $\mathcal{O}(0.1)$ CP-violating phase in the Yukawa interaction between H_1 (the 125 GeV Higgs boson) and fermions is still allowed. For these scenarios, we study CP-violating effects in the neutron EDM and $t\bar{t}H_1$ production at the LHC. Our analysis shows that such an $\mathcal{O}(0.1)$ CP-violating phase can be easily confirmed or excluded by future neutron EDM tests with LHC data providing a complementary cross-check.

Contents

1	Introduction	2
2	Model Set-up	3
3	Current EDM Constraints and Future Tests	6
3.1	Electron EDM	6
3.2	Neutron EDM	10
3.3	Numerical Analysis for the 2HDM	12
3.4	Future Neutron EDM Tests	16
3.5	Summary on EDM Tests	17
4	Current Collider Constraints	18
4.1	Global Fit on Higgs Signal Strengths	18
4.2	LHC Direct Searches for Heavy Scalars	22
4.3	Summary on Collider Constraints	26
5	LHC Phenomenology of CP-violation in $t\bar{t}H_1$ Production	26
5.1	Phenomenological Setup	26
5.2	Inclusive $t\bar{t}H_1$ Cross Section	27
5.3	Results	29
6	Conclusions	31
A	Yukawa Couplings	32
B	Scalar Couplings	34
C	Loop Integrations for EDM	35
D	Loop Integrations for Higgs Production and Decay	36
E	Decay of Heavy (Pseudo)scalars	37
F	CP-violation Observables in the $t\bar{t}H_1$ Channel	38
G	Top Quark Reconstruction	40

1 Introduction

CP-violation was first discovered in 1964 through the $K_L \rightarrow \pi\pi$ rare decay channel [1]. Later, more CP-violation effects were discovered in the K-, B-, and D-meson sectors [2, 3] and all the discovered effects are consistent with the explanation given by the Kobayashi-Maskawa (KM) mechanism [4]. However, the KM mechanism itself cannot generate a large enough matter-antimatter asymmetry in the Universe. Therefore, new CP-violation sources beyond the KM mechanism are needed to explain the latter [5–8].

Experimentally, all the discovered effects of CP-violation till now have appeared in flavor physics measurements, yet they can also be tested through other methods. These can generally be divided into two different categories: (a) indirect tests, which can merely probe the existence of CP-violation but cannot confirm the source(s) behind it; (b) direct tests, which can directly lead us to the actual CP-violation interaction(s).

For indirect tests, there is a typical example that one most often uses, the Electric Dipole Moment (EDM) measurements [9–13]. The reason is that the EDM effective interaction of a fermion is

$$\mathcal{L}_{\text{EDM}} = -\frac{i}{2} d_f \bar{f} \sigma^{\mu\nu} \gamma^5 f F_{\mu\nu}, \quad (1.1)$$

wherein d_f is the EDM of such a fermion f , which leads to P- and CP-violation simultaneously [10]. It is a pure quantum effect, i.e., emerging at loop level and, in the Standard Model (SM), the electron and neutron EDMs are predicted to be extremely small [10],

$$|d_e^{\text{SM}}| \sim 10^{-38} e \cdot \text{cm}, \quad |d_n^{\text{SM}}| \sim 10^{-38} e \cdot \text{cm}, \quad (1.2)$$

because they are generated at four- or three-loop level, respectively. Thus, since the SM predictions for these are still far below the recent experimental limits [14–17]

$$|d_e| < 1.1 \times 10^{-29} e \cdot \text{cm}, \quad |d_n| < 1.8 \times 10^{-26} e \cdot \text{cm}, \quad (1.3)$$

both given at 90% Confidence Level (C.L.)¹, these EDMs provide a fertile ground to test the possibility of CP-violation due to new physics. In fact, in some Beyond the SM (BSM) scenarios, the EDMs of the electron and neutron can be generated already at one- or two-loop level, thus these constructs may be already strictly constrained or excluded. In measurements of d_e and d_n , though, even if we discover that either or both EDMs are far above the SM predictions, we cannot determine the exact interaction which constitutes such a CP-violation.

For direct tests, there are several typical channels to test CP-violation at colliders. For instance, measuring the final state distributions from top pair [18–27] or τ pair [28–34] production enables one to test CP-violating effects entering the interactions of the fermions with one or more Higgs bosons. The discovery of the 125 GeV Higgs boson [35–37] makes such experiments feasible. Indeed, if more (pseudo)scalar (or else new vector) states are

¹An earlier result [15, 16] is $|d_n| < 3.0 \times 10^{-26} e \cdot \text{cm}$ while a most recent measurement by the nEDM group [17] set a stricter constraint $|d_n| < 1.8 \times 10^{-26} e \cdot \text{cm}$, both at 90% C.L. At 95% C.L., the latest constraint is then $|d_n| < 2.2 \times 10^{-26} e \cdot \text{cm}$.

discovered, one can also try to measure the couplings amongst (old and new) scalars and vectors themselves to probe CP-violation entirely from the bosonic sector [38–40]. At high energy colliders, the discovery of some CP-violation effects can lead us directly to the CP-violating interaction(s), essentially because herein one can produce final states that can be studied at the differential level, thanks to the ability of the detectors to reconstruct their (at times, full) kinematics, which can then be mapped to both cross section and (charge/spin) asymmetry observables.

Theoretically, new CP-violation can appear in many new physics models, for example, those with an extended Higgs sector [41–46]. Among these, we choose to deal here with the widely studied 2-Higgs-Doublet Model (2HDM) [45], which we use as a prototypical source of CP-violation entertaining both direct and indirect tests of it. Specifically, the 2HDM with a Z_2 symmetry is used here, in order to avoid large Flavor Changing Neutral Currents (FCNCs) [45], yet such a symmetry must be softly broken if one wants CP-violation to arise in this scenario. We will therefore study the effects of such a CP-violating 2HDM onto (electron and neutron) EDMs as well as processes entering the Large Hadron Collider (LHC), specifically, those involving the production of a top-antitop pair in association with the 125 GeV Higgs boson.

This paper is organized as follows. In [section 2](#), we review the construction of the 2HDM with so-called “soft” CP-violation with the four standard types of Yukawa interactions. Then, in [section 3](#), we discuss the current constraints from electron and neutron EDMs, show the reason why we eventually choose to pursue phenomenologically only the 2HDM Type II and Type III for our collider analysis and discuss the importance of future neutron EDM tests. In [section 4](#), we discuss the current constraints from collider experiments on these two realizations of a 2HDM. In [section 5](#), we discuss LHC phenomenology studies on CP-violation effects in the $t\bar{t}H_1$ associated production process. Finally, we summarize and conclude in [section 6](#). There are also several appendices which we use to collect technical details.

2 Model Set-up

In this section, we briefly review the 2HDM with a softly broken Z_2 symmetry and how CP-violation arises in such a model. We mainly follow the conventions in [47–49]. The Lagrangian of the scalar sector can be written as

$$\mathcal{L} = \sum_{i=1,2} (D_\mu \phi_i)^\dagger (D^\mu \phi_i) - V(\phi_1, \phi_2). \quad (2.1)$$

Under a Z_2 transformation, we can have $\phi_1 \rightarrow \phi_1$, $\phi_2 \rightarrow -\phi_2$, thus, in the scalar potential, all terms must contain even numbers of ϕ_i . However, if the Z_2 symmetry is softly broken,

a term $\propto \phi_1^\dagger \phi_2$ is allowed, thus the scalar potential becomes

$$V(\phi_1, \phi_2) = -\frac{1}{2} \left[m_1^2 \phi_1^\dagger \phi_1 + m_2^2 \phi_2^\dagger \phi_2 + \left(m_{12}^2 \phi_1^\dagger \phi_2 + \text{H.c.} \right) \right] + \frac{1}{2} \left[\lambda_1 \left(\phi_1^\dagger \phi_1 \right)^2 + \lambda_2 \left(\phi_2^\dagger \phi_2 \right)^2 \right] \\ + \lambda_3 \left(\phi_1^\dagger \phi_1 \right) \left(\phi_2^\dagger \phi_2 \right) + \lambda_4 \left(\phi_1^\dagger \phi_2 \right) \left(\phi_2^\dagger \phi_1 \right) + \left[\frac{\lambda_5}{2} \left(\phi_1^\dagger \phi_2 \right)^2 + \text{H.c.} \right]. \quad (2.2)$$

Here $\phi_{1,2}$ are SU(2) scalar doublets, which are defined as

$$\phi_1 \equiv \begin{pmatrix} \varphi_1^+ \\ \frac{v_1 + \eta_1 + i\chi_1}{\sqrt{2}} \end{pmatrix}, \quad \phi_2 \equiv \begin{pmatrix} \varphi_2^+ \\ \frac{v_2 + \eta_2 + i\chi_2}{\sqrt{2}} \end{pmatrix}. \quad (2.3)$$

The parameters $m_{1,2}^2$ and $\lambda_{1,2,3,4}$ must be real, while m_{12}^2 and λ_5 can be complex. Further, $v_{1,2}$ are the Vacuum Expectation Values (VEVs) of the scalar doublets with the relation $\sqrt{|v_1|^2 + |v_2|^2} = 246$ GeV. The ratio v_2/v_1 may also be complex², and we define $t_\beta \equiv |v_2/v_1|$ as usual³.

As was shown in [45], CP-violation in the scalar sector requires a nonzero m_{12}^2 . For the three possible complex parameters m_{12}^2 , λ_5 , and v_2/v_1 , we can always perform a field rotation to keep at least one of them real. In this paper, we choose v_2/v_1 to be real (thus both $v_{1,2}$ are real) like in [47–49], and have the relation

$$\text{Im}(m_{12}^2) = v_1 v_2 \text{Im}(\lambda_5) \quad (2.4)$$

following the minimization conditions for the scalar potential. If $\text{Im}(m_{12}^2)$ and $\text{Im}(\lambda_5)$ are non-zero, CP-violation occurs in the scalar sector.

We diagonalize the charged components as

$$\begin{pmatrix} G^+ \\ H^+ \end{pmatrix} = \begin{pmatrix} c_\beta & s_\beta \\ -s_\beta & c_\beta \end{pmatrix} \begin{pmatrix} \varphi_1^+ \\ \varphi_2^+ \end{pmatrix}, \quad (2.5)$$

where H^+ is the charged Higgs boson and G^+ is the charged Goldstone. Similarly, for the CP-odd neutral components,

$$\begin{pmatrix} G^0 \\ A \end{pmatrix} = \begin{pmatrix} c_\beta & s_\beta \\ -s_\beta & c_\beta \end{pmatrix} \begin{pmatrix} \chi_1 \\ \chi_2 \end{pmatrix}, \quad (2.6)$$

where A is the physical CP-odd degree of freedom and G^0 is the neutral Goldstone. In the CP-conserved case, A is a pseudoscalar boson while, in the CP-violating case, A has further mixing with the CP-even degrees of freedom as

$$\begin{pmatrix} H_1 \\ H_2 \\ H_3 \end{pmatrix} = R \begin{pmatrix} \eta_1 \\ \eta_2 \\ A \end{pmatrix}. \quad (2.7)$$

²We can always fix v_1 real through gauge transformation and v_2 may be complex at the same time.

³In this paper, we denote $s_\alpha \equiv \sin \alpha$, $c_\alpha \equiv \cos \alpha$, and $t_\alpha \equiv \tan \alpha$.

Here $H_{1,2,3}$ are mass eigenstates and we choose H_1 as the lightest one with mass $m_1 = 125$ GeV, so that it is the discovered SM-like Higgs boson. The rotation matrix R can be parameterized as

$$R = \begin{pmatrix} 1 & & \\ & c_{\alpha_3} & s_{\alpha_3} \\ & -s_{\alpha_3} & c_{\alpha_3} \end{pmatrix} \begin{pmatrix} c_{\alpha_2} & s_{\alpha_2} \\ & 1 \\ -s_{\alpha_2} & c_{\alpha_2} \end{pmatrix} \begin{pmatrix} c_{\beta+\alpha_1} & s_{\beta+\alpha_1} \\ -s_{\beta+\alpha_1} & c_{\beta+\alpha_1} \\ & & 1 \end{pmatrix}. \quad (2.8)$$

When $\alpha_{1,2} \rightarrow 0$, H_1 becomes the SM Higgs boson. If $m_{1,2}$, $\alpha_{1,2,3}$ and β are known, m_3 can be expressed as

$$m_3^2 = \frac{(m_1^2 - m_2^2 s_{\alpha_3}^2) c_{2\beta+\alpha_1} / c_{\alpha_3}^2 - m_2^2 s_{2\beta+\alpha_1} t_{\alpha_3}}{c_{2\beta+\alpha_1} s_{\alpha_2} - s_{2\beta+\alpha_1} t_{\alpha_3}}. \quad (2.9)$$

In the mass eigenstates, the couplings between neutral scalars and gauge bosons can be parameterized via

$$\begin{aligned} \mathcal{L} \supset & \sum_{1 \leq i \leq 3} c_{V,i} H_i \left(\frac{2m_W^2}{v} W^{+,\mu} W_\mu^- + \frac{m_Z^2}{v} Z^\mu Z_\mu \right) \\ & + \sum_{i=1}^3 \frac{c_{ij} g}{2c_{\theta_W}} Z_\mu (H_i \partial^\mu H_j - H_j \partial^\mu H_i). \end{aligned} \quad (2.10)$$

The coefficients are then

$$c_{V,1} = c_{23} = c_{\alpha_1} c_{\alpha_2}, \quad (2.11)$$

$$c_{V,2} = -c_{13} = -c_{\alpha_3} s_{\alpha_1} - c_{\alpha_1} s_{\alpha_2} s_{\alpha_3}, \quad (2.12)$$

$$c_{V,3} = c_{12} = s_{\alpha_1} s_{\alpha_3} - c_{\alpha_1} c_{\alpha_3} s_{\alpha_2}. \quad (2.13)$$

Next we turn to the Yukawa sector. Due to the Z_2 symmetry, a fermion bilinear can couple to only one scalar doublet, with the form $\bar{Q}_L \phi_i D_R$, $\bar{Q}_L \tilde{\phi}_i U_R$, or $\bar{L}_L \phi_i \ell_R$, thus it is helpful to avoid the FCNC problem [45]. Here $\tilde{\phi}_i \equiv i\sigma_2 \phi_i^*$ and left-handed fermion doublets are defined as $Q_{i,L} \equiv (U_i, D_i)_L^T$ and $L_L \equiv (\nu_i, \ell_i)_L^T$, for the i -th generation. Since the scalar potential contains a $\phi_1 \leftrightarrow \phi_2$ exchange symmetry, we can set the convention in which $\bar{Q}_L U_R$ always couple to ϕ_2 so that there are four standard types of Yukawa couplings [45, 49]:

$$\mathcal{L} \supset \begin{cases} -Y_U \bar{Q}_L \tilde{\phi}_2 U_R - Y_D \bar{Q}_L \phi_2 D_R - Y_\ell \bar{L}_L \phi_2 \ell_R + \text{H.c.}, & \text{(Type I)}, \\ -Y_U \bar{Q}_L \tilde{\phi}_2 U_R - Y_D \bar{Q}_L \phi_1 D_R - Y_\ell \bar{L}_L \phi_1 \ell_R + \text{H.c.}, & \text{(Type II)}, \\ -Y_U \bar{Q}_L \tilde{\phi}_2 U_R - Y_D \bar{Q}_L \phi_2 D_R - Y_\ell \bar{L}_L \phi_1 \ell_R + \text{H.c.}, & \text{(Type III)}, \\ -Y_U \bar{Q}_L \tilde{\phi}_2 U_R - Y_D \bar{Q}_L \phi_1 D_R - Y_\ell \bar{L}_L \phi_2 \ell_R + \text{H.c.}, & \text{(Type IV)}. \end{cases} \quad (2.14)$$

The fermion mass matrix is $M_f = Y_f v c_\beta / \sqrt{2}$ if the fermion couples to ϕ_1 and $M_f = Y_f v s_\beta / \sqrt{2}$ if it couples to ϕ_2 . We parameterize the Yukawa couplings of mass eigenstates as

$$\mathcal{L} \supset - \sum_{i,f} \frac{m_f}{v} (c_{f,i} H_i \bar{f}_L f_R + \text{H.c.}). \quad (2.15)$$

For CP-violating models, $c_{f,i}$ are complex numbers and we list them in [Appendix A](#) for all four types of Yukawas. In all these models, $\text{Im}(c_{f,1}) \propto s_{\alpha_2}$, thus α_2 is an important mixing angle which measures the CP-violating phase in the Yukawa couplings of H_1 .

3 Current EDM Constraints and Future Tests

In this section, we analyze the EDM constraints of the electron and neutron for the four types of 2HDM in some detail. The $b \rightarrow s\gamma$ decay requires the charged Higgs mass to be $m_{H^\pm} \gtrsim 600$ GeV for all the four types of Yukawa couplings when $t_\beta \sim 1$ [[50](#), [51](#)]. If t_β gets larger, the constraints will become weaker for Type I and III Yukawa couplings. The oblique parameters [[52](#), [53](#)] will then favor the case $m_{H_{2,3}} \gtrsim 500$ GeV [[54–57](#)]⁴. With such choices for the scalar masses, the vacuum stability condition favors $\mu^2 \equiv \text{Re}(m_{12}^2)/s_{2\beta} \lesssim (450 \text{ GeV})^2$ [[48](#)]. Notice that μ^2 will modify the charged Higgs couplings a little, but it is not numerically important to the EDM calculation, so we fix it at $\mu^2 = (450 \text{ GeV})^2$ in the rest of this work. More discussions about the scalar couplings will appear in [Appendix B](#).

An electron EDM measurement places a very strict constraint on the complex Yukawa couplings in most models. As a rough estimation, if we consider CP-violation only in the 125 GeV Higgs interaction with the top quark, the typical constraint is $\arg(c_{t,1}) \lesssim 10^{-3}$ [[58](#)]. However, some models (including the 2HDM) allow for the accidental cancellation among various contributions, so that larger $\arg(c_{t,1})$ may still be allowed [[59–64](#)]. In such cases, neutron EDM constraints will also become important, as shown in the analysis later in this section.

3.1 Electron EDM

A recent electron EDM measurement was performed using the ThO molecule [[14](#)]. The exact constrained quantity is

$$|d_e^{\text{eff}}| \equiv |d_e + kC| < 1.1 \times 10^{-29} e \cdot \text{cm}. \quad (3.1)$$

The second term measures the contribution from CP-violating electron-nucleon interactions via

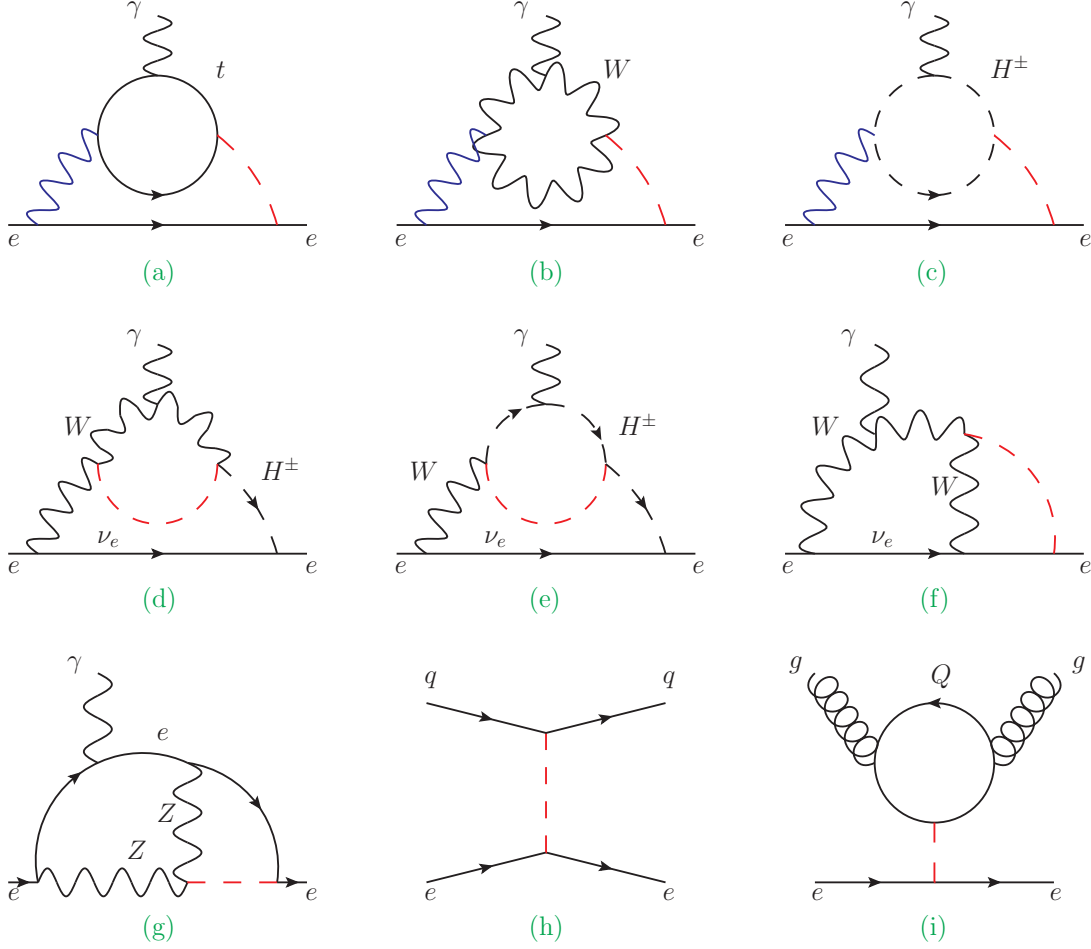
$$\mathcal{L} \supset C (\bar{N}N) (\bar{e}i\gamma^5 e), \quad (3.2)$$

where the coefficient C is almost the same for proton and neutron. Here, $k \approx 1.6 \times 10^{-15} \text{ GeV}^2 e \cdot \text{cm}$, which was obtained for ThO [[65](#), [66](#)], however, for most other materials with heavy atoms, this quantity appears to be of the same order [[10](#), [67](#)]. The contribution from electron-nucleon interactions is usually sub-leading, though it can also become important.

The typical Feynman diagrams contributing to the electron EDM in the 2HDM are listed in [Figure 1](#). Diagrams (a)-(e) are Barr-Zee type diagrams [[68](#)] with the top quark t , W^\pm -boson, or charged Higgs H^\pm in the upper loop, while diagrams (f) and (g) are non-Barr-Zee type. Such seven diagrams contribute directly to d_e . Diagram (h) shows the

⁴When H_1 is SM-like, the oblique parameter constraints are sensitive mainly to the mass splitting between the charged and neutral scalars. They are not sensitive to the mixing parameters in [Equation 2.8](#).

Figure 1. Typical Feynman diagrams contributing to the electron EDM in the 2HDM. The blue lines can be γ or Z while red lines are neutral Higgses $H_{1,2,3}$. Diagrams (a)-(g) will contribute to d_e directly while diagrams (h)-(i) will contribute to the electron-nucleon interaction term.



contribution through the electron-quark interaction, while diagram (i) shows the contribution through the electron-gluon interaction. The contributions can be divided into eight parts as summarized in [Table 1](#).

The analytical expressions in the Feynman-'t Hooft gauge are listed below. For simplicity we denote

$$\delta_0 \equiv \frac{\sqrt{2}m_e G_F \alpha_{\text{em}}}{(4\pi)^3} = 3.1 \times 10^{-14} \text{ GeV} = 6.1 \times 10^{-28} e \cdot \text{cm} \quad (3.3)$$

from now on. For the fermion-loop contribution in which the top quark is dominant, we

Table 1. Different contributions to the electron EDM and the corresponding Feynman diagrams.

	Diagram	Contribution	CP-violation vertex
$d_e^{t,\gamma/Z,H_i}$	(a)	Fermion (top) loop	$H_i\bar{e}e, H_i\bar{t}t$
$d_e^{W,\gamma/Z,H_i}$	(b)	W -loop	$H_i\bar{e}e$
$d_e^{H^\pm,\gamma/Z,H_i}$	(c)	Charged Higgs H^\pm loop	$H_i\bar{e}e$
d_e^{W,H^\pm,H_i}	(d) and (e)	W^\pm - H^\pm -loop	$H^\pm W^\mp H_i$
δd_e^W	(f)	non-Barr-Zee W -loop	$H_i\bar{e}e$
δd_e^Z	(g)	non-Barr-Zee Z -loop	$H_i\bar{e}e$
$d_{e,q,i}^{\text{int}}$	(h)	Electron-quark interaction	$H_i\bar{e}e$
$d_{e,g,i}^{\text{int}}$	(i)	Electron-gluon interaction	$H_i\bar{e}e$

have [68–74]

$$\frac{d_e^{t,\gamma,H_i}}{e} = \frac{32}{3}\delta_0 [f(z_{tH_i})\text{Re}(c_{t,i})\text{Im}(c_{e,i}) + g(z_{tH_i})\text{Re}(c_{e,i})\text{Im}(c_{t,i})], \quad (3.4)$$

$$\frac{d_e^{t,Z,H_i}}{e} = -\frac{\left(1 - \frac{8s_{\theta_W}^2}{3}\right)(-1 + 4s_{\theta_W}^2)}{s_{\theta_W}^2 c_{\theta_W}^2}\delta_0 \times [F(z_{tH_i}, z_{tZ})\text{Re}(c_{t,i})\text{Im}(c_{e,i}) + G(z_{tH_i}, z_{tZ})\text{Re}(c_{e,i})\text{Im}(c_{t,i})]. \quad (3.5)$$

Here $z_{ij} \equiv m_i^2/m_j^2$ and θ_W is the weak mixing angle with $s_{\theta_W}^2 = 0.23$. The loop integration functions here and below are all listed in [Appendix C](#). For the electron EDM calculation, the Z -mediated contribution is accidentally suppressed by $-1/2 + 2s_{\theta_W}^2 \sim -0.04$. For the W -loop contribution, we have [68–74]

$$\frac{d_e^{W,\gamma,H_i}}{e} = -\delta_0 \left[12f(z_{WH_i}) + 23g(z_{WH_i}) + 3h(z_{WH_i}) + \frac{2}{z_{WH_i}}(f(z_{WH_i}) - g(z_{WH_i})) \right] c_{V,i}\text{Im}(c_{e,i}), \quad (3.6)$$

$$\frac{d_e^{W,Z,H_i}}{e} = \frac{-1 + 4s_{\theta_W}^2}{s_{\theta_W}^2}\delta_0 \left[\frac{5 - t_{\theta_W}^2}{2}F(z_{WH_i}, c_{\theta_W}^2) + \frac{7 - 3t_{\theta_W}^2}{2}G(z_{WH_i}, c_{\theta_W}^2) + \frac{3}{4}h(z_{WH_i}) + \frac{3}{4}g(z_{WH_i}) + \frac{1 - t_{\theta_W}^2}{4z_{WH_i}}(F(z_{WH_i}, c_{\theta_W}^2) - G(z_{WH_i}, c_{\theta_W}^2)) \right] c_{V,i}\text{Im}(c_{e,i}). \quad (3.7)$$

This contribution will cross zero around $m_i \sim 500$ GeV because of the cancellation between W and Goldstone contributions and, in the heavy m_i limit, the pure Goldstone diagram

has the behavior $\sim \ln(m_i^2/m_W^2)$. The charged Higgs loop contributions are [71]

$$\frac{d_e^{H^\pm, \gamma, H_i}}{e} = - \left(\frac{2\delta_0 v^2}{m_\pm^2} \right) [f(z_{\pm, i}) - g(z_{\pm, i})] c_{\pm, i} \text{Im}(c_{e, i}), \quad (3.8)$$

$$\frac{d_e^{H^\pm, Z, H_i}}{e} = \frac{-1 + 4s_{\theta_W}^2}{s_{2\theta_W} t_{2\theta_W}} \left(\frac{2\delta_0 v^2}{m_\pm^2} \right) [F(z_{\pm, i}, z_{\pm, Z}) - G(z_{\pm, i}, z_{\pm, Z})] c_{\pm, i} \text{Im}(c_{e, i}). \quad (3.9)$$

Hereafter, “ \pm ” is used to denote the charged Higgs boson while $c_{\pm, i}$ is the coupling constant between the charged and neutral scalars entering via $\mathcal{L} \supset -c_{\pm, i} v H_i H^+ H^-$. The W^\pm - H^\pm associated loop yields [71]

$$\frac{d_e^{W, H^\pm, H_i}}{e} = - \frac{\delta_0}{2s_{\theta_W}^2} \left[\frac{H_i^a(z_{WH_i}) - H_i^a(z_{\pm, i})}{z_{\pm, W} - 1} c_{V, i} - \frac{H_i^b(z_{WH_i}) - H_i^b(z_{\pm, i})}{z_{\pm, W} - 1} c_{\pm, i} \right] \text{Im}(c_{e, i}). \quad (3.10)$$

The first term corresponds to diagram (d) while the second term corresponds to diagram (e). The non-Barr-Zee type diagrams give [70, 74]⁵

$$\frac{d_e^{W, H_i}}{e} = - \frac{\delta_0}{s_{\theta_W}^2} \left(D_{W, i}^a + D_{W, i}^b + D_{W, i}^c + D_{W, i}^d + D_{W, i}^e \right) c_{V, i} \text{Im}(c_{e, i}), \quad (3.11)$$

$$\frac{d_e^{Z, H_i}}{e} = -4\delta_0 t_{\theta_W}^2 \left(D_{Z, i}^a + D_{Z, i}^b + D_{Z, i}^c \right) c_{V, i} \text{Im}(c_{e, i}). \quad (3.12)$$

The analytical expressions are too lengthy to present them here so that we list all of them in [Appendix C](#). The interaction induced effective EDM terms are [66, 75–77]

$$d_{e, q, i}^{\text{int}} = \frac{\sqrt{2} m_e G_F k}{m_i^2} \text{Im}(c_{e, i}) \left[\text{Re}(c_{u, i}) \langle m_u \bar{u} u \rangle + \text{Re}(c_{d, i}) (\langle m_d \bar{d} d \rangle + \langle m_s \bar{s} s \rangle) \right], \quad (3.13)$$

$$d_{e, g, i}^{\text{int}} = - \frac{\sqrt{2} m_e G_F k}{3m_i^2} \text{Im}(c_{e, i}) [2\text{Re}(c_{u, i}) + \text{Re}(c_{d, i})] \left\langle \frac{\alpha_s}{4\pi} G_{\mu\nu} G^{\mu\nu} \right\rangle. \quad (3.14)$$

The nucleon matrix elements $\langle \mathcal{O} \rangle \equiv \langle N | \mathcal{O} | N \rangle$ and their values are similar for proton and neutron. Thus we choose the average values of proton and neutron considering three active quarks (u, d, s) at the hadron scale ~ 1 GeV [77–81], as listed in [Table 2](#). Summing all

Table 2. Nucleon matrix elements in the 3-flavor scheme at the hadron scale ~ 1 GeV. The quark matrix elements were obtained from lattice calculation [80] while the gluon matrix element was derived based on [81].

$\langle m_u \bar{u} u \rangle$	$\langle m_d \bar{d} d \rangle$	$\langle m_s \bar{s} s \rangle$	$\langle \frac{\alpha_s}{4\pi} G_{\mu\nu} G^{\mu\nu} \rangle$
14.5 MeV	31.4 MeV	40.2 MeV	-183 MeV

⁵We have checked the results in [70] and [74]. In the heavy m_i limit, the loop functions should be logarithm enhanced as in [70] (just like the pure Goldstone contribution in [69]). However, the results in [74] have improper power enhancement thus this behavior cannot be physical. So we used for validation the result in [70].

parts together, the effective electron EDM is

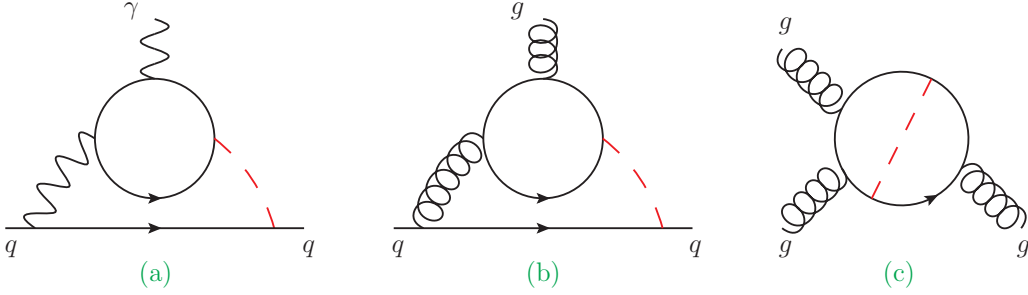
$$\begin{aligned}
d_e^{\text{eff}} &= d_e + d_e^{\text{int}} \\
&= d_e^{t,\gamma,H_i} + d_e^{t,Z,H_i} + d_e^{W,\gamma,H_i} + d_e^{W,Z,H_i} + d_e^{H^\pm,\gamma,H_i} + d_e^{H^\pm,Z,H_i} + d_e^{W,H^\pm,H_i} \\
&\quad + \delta d_e^W + \delta d_e^Z + d_{e,q,i}^{\text{int}} + d_{e,g,i}^{\text{int}}.
\end{aligned} \tag{3.15}$$

For each part above, $d_e^j \propto m_e$ thus it is suppressed by the small electron mass. We can extract $C_e^j \equiv d_e^j/(-m_e)$, which is independent of the fermion mass. This coefficient is not useful in the electron EDM calculation, but it will be helpful in order to map the corresponding part into the quark EDM, which is important in the neutron EDM calculation below.

3.2 Neutron EDM

The neutron EDM calculation is more complex as it involves more contributions and QCD effects. As shown in [Figure 2](#), there are three types of operators contributing to the neutron

Figure 2. Various contributions to the neutron EDM: quark EDM, quark Color EDM (CEDM) and Weinberg operator.



EDM, including the quark EDM operator \mathcal{O}_q , quark CEDM operator $\tilde{\mathcal{O}}_q$ and Weinberg operator \mathcal{O}_g . They are chosen as follows: [10, 72]

$$\mathcal{O}_q = -\frac{i}{2} e Q_q m_q \bar{q} \sigma^{\mu\nu} \gamma_5 q F_{\mu\nu}, \tag{3.16}$$

$$\tilde{\mathcal{O}}_q = -\frac{i}{2} g_s m_q \bar{q} \sigma^{\mu\nu} t^a \gamma_5 q G_{\mu\nu}^a, \tag{3.17}$$

$$\mathcal{O}_g = -\frac{1}{3} g_s f^{abc} G_{\mu\rho}^a G_\nu^{b,\rho} \tilde{G}^{c,\mu\nu}, \tag{3.18}$$

where g_s is the QCD coupling constant, t^a is a generator of the QCD group and f^{abc} denotes a QCD structure constant. At a scale μ ,

$$\mathcal{L} \supset \sum_{q=u,d} \left(C_q(\mu) \mathcal{O}_q(\mu) + \tilde{C}_q(\mu) \tilde{\mathcal{O}}_q(\mu) \right) + C_g(\mu) \mathcal{O}_g(\mu) \tag{3.19}$$

and

$$d_q(\mu)/e \equiv Q_q m_q(\mu) C_q(\mu), \quad \tilde{d}_q(\mu) \equiv m_q(\mu) \tilde{C}_q(\mu). \tag{3.20}$$

For convenience we also redefine $w(\mu) \equiv g_s(\mu)C_g(\mu)$. Notice that these EDMs should be first calculated at the weak scale $\mu_W \sim m_t$.

The calculation methods of C_u and C_d are the same as those for d_e through diagrams (a)-(g) in [Figure 1](#). For the quark EDM, we perform the calculation at the weak scale $\mu_W \approx m_t$ and list the results of the C_q^j evaluation [[71](#)] as follows:

$$C_q^{t/W/H^\pm, \gamma, H_i}, \delta C_q^Z = \bar{C}_e^{t/W/H^\pm, \gamma, H_i}, \delta \bar{C}_e^Z, \quad (3.21)$$

$$C_d^{t/W/H^\pm, Z, H_i} = \frac{-\frac{1}{2} + \frac{2s_{\theta_W}^2}{3}}{-\frac{1}{2} + 2s_{\theta_W}^2} \cdot \frac{-1}{Q_d} \bar{C}_e^{t/W/H^\pm, Z, H_i}, \quad (3.22)$$

$$C_u^{t/W/H^\pm, Z, H_i} = \frac{\frac{1}{2} - \frac{4s_{\theta_W}^2}{3}}{-\frac{1}{2} + 2s_{\theta_W}^2} \cdot \frac{-1}{Q_u} \bar{C}_e^{t/W/H^\pm, Z, H_i}, \quad (3.23)$$

$$C_u^{W, H^\pm, H_i}, \delta C_u^W = \frac{1}{Q_u} \bar{C}_e^{W, H^\pm, H_i}, \frac{1}{Q_u} \delta \bar{C}_e^W, \quad (3.24)$$

$$C_d^{W, H^\pm, H_i}, \delta C_d^W = \frac{-1}{Q_d} \bar{C}_e^{W, H^\pm, H_i}, \frac{-1}{Q_d} \delta \bar{C}_e^W. \quad (3.25)$$

Here, each \bar{C}_e^j means C_e^j with a replacement $c_{e,i} \rightarrow c_{q,i}$ in the Yukawa couplings. The contributions including the Z boson in the Bar-Zee diagram become important in the quark EDM calculation, because there is no accidental suppression like that in the electron EDM calculation. For the CEDM terms, only Barr-Zee diagrams with a top loop contribute. The result at the weak scale $\mu_W \sim m_t$ is then [[71](#), [72](#)]

$$\tilde{C}_q(\mu_W) = -\frac{2\sqrt{2}\alpha_s(\mu_W)G_F}{(4\pi)^3} \sum_{i=1}^3 [f(z_{tH_i})\text{Re}(c_{U,i})\text{Im}(c_{q,i}) + g(z_{tH_i})\text{Re}(c_{q,i})\text{Im}(c_{U,i})]. \quad (3.26)$$

The coefficient of the Weinberg operator at weak scale is [[10](#), [72](#)]

$$C_g(\mu_W) = \frac{\sqrt{2}\alpha_s(\mu_W)G_F}{4(4\pi)^3} \sum_{i=1}^3 W(z_{tH_i})\text{Re}(c_{U,i})\text{Im}(c_{U,i}), \quad (3.27)$$

and the loop integration $W(z)$ is listed in [Appendix C](#).

To calculate the EDM of the neutron, we must consider the QCD running effects to evolve these to the hadron scale $\mu_H \sim 1$ GeV. The one-loop running gives [[72](#), [82–85](#)]

$$\begin{pmatrix} C_q(\mu_H) \\ \tilde{C}_q(\mu_H) \\ C_g(\mu_H) \end{pmatrix} = \begin{pmatrix} 0.42 & -0.38 & -0.07 \\ & 0.47 & 0.15 \\ & & 0.20 \end{pmatrix} \begin{pmatrix} C_q(\mu_W) \\ \tilde{C}_q(\mu_W) \\ C_g(\mu_W) \end{pmatrix}. \quad (3.28)$$

There is no quark mass dependence in C_q or \tilde{C}_q and the evolution of C_g is equivalent to $w(\mu_H) = 0.41w(\mu_W)$. According to [Equation 3.20](#), we only need the quark mass parameters

at $\mu_H \sim 1$ GeV in the final calculation. The one-loop running mass effect is [2]

$$m_q(1 \text{ GeV})/m_q(2 \text{ GeV}) = 1.38 \quad (3.29)$$

and, with the lattice results at 2 GeV [2, 86, 87], we have

$$m_u(1 \text{ GeV}) \simeq 3.0 \text{ MeV}, \quad m_d(1 \text{ GeV}) \simeq 6.5 \text{ MeV}. \quad (3.30)$$

The hadron scale estimation was performed based on QCD sum rules [10, 72, 88, 89]⁶

$$\frac{d_n}{e} \simeq (22 \text{ MeV})w(\mu_H) + 0.65\frac{d_d(\mu_H)}{e} - 0.16\frac{d_u(\mu_H)}{e} + 0.48\tilde{d}_d(\mu_H) + 0.24\tilde{d}_u(\mu_H), \quad (3.31)$$

with an uncertainty of about 50%. Combining all these results above, we have

$$\begin{aligned} \frac{d_n}{e} = & m_d(\mu_H) \left(0.27Q_d C_d(\mu_W) + 0.31\tilde{C}_d(\mu_W) \right) \\ & + m_u(\mu_H) \left(-0.07Q_u C_u(\mu_W) + 0.16\tilde{C}_u(\mu_W) \right) + (9.6 \text{ MeV}) w(\mu_W). \end{aligned} \quad (3.32)$$

3.3 Numerical Analysis for the 2HDM

In this section we analyze the 2HDM with soft CP-violation, including all the four types of Yukawa interactions. For the electron EDM, the Type I and IV models give the same results, while the Type II and III models give the same results⁷.

For Type I and IV models, numerical results show that there is no cancellation among various contributions to the electron EDM, thus the CP-violating phase is strictly constrained. This behavior is consistent with the results in which only the contribution from H_1 is considered [58]. We take $m_{2,3} \sim 500$ GeV and $m_{\pm} \sim 600$ GeV as a benchmark point and find

$$d_e^{\text{I,IV}} \simeq -1.3 \times 10^{-26} s_{\alpha_2}/t_{\beta} \quad (3.33)$$

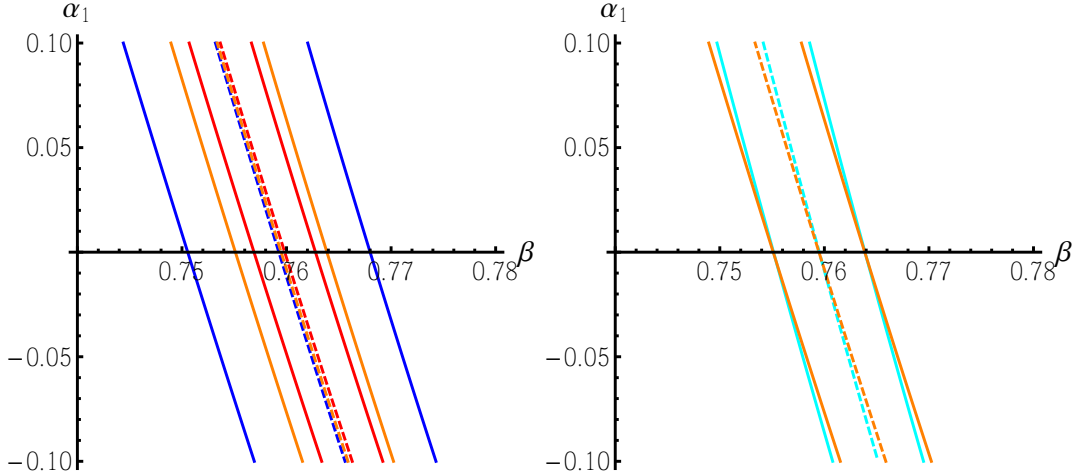
in the region $t_{\beta} \sim (1-10)$. This result is not sensitive to $\alpha_{1,3}$ and gives $|s_{\alpha_2}/t_{\beta}| \lesssim 8.5 \times 10^{-4}$, which means the CP-phase $|\arg(c_{f,1})| \lesssim 8.5 \times 10^{-4}$ for $f = \ell_i, U_i$. This is extremely small and would not be able to produce interesting CP-violating effects, so in the rest of this work, we do not discuss further these two 2HDM realizations.

For Type II and III models, in contrast, numerical results show significant cancellation behavior for some parameter regions in the electron EDM calculation and thus α_2 is allowed to reach $\mathcal{O}(0.1)$. For these two models, we can discuss two different scenarios: (a) the heavy neutral scalars $H_{2,3}$ are close in mass and α_3 can be changed in a wide range; (b) H_2 and H_3 have large mass splitting, and thus α_3 must be close to 0 or $\pi/2$.

⁶The light quark condensation is chosen as $\langle \bar{q}q \rangle(1 \text{ GeV}) = -(254 \text{ MeV})^3$ [90], which is a bit larger than that from [10, 88]. Ref. [90] presents the lattice result $\langle \bar{q}q \rangle(2 \text{ GeV}) = -(283 \text{ MeV})^3$ and also shows the Renormalization Group Equation (RGE) running effect as $d\langle m_q \bar{q}q \rangle(\mu)/d\ln \mu \propto m_q^4$, which is negligible for u and d quarks. Thus we have $\langle \bar{q}q \rangle(1 \text{ GeV})/\langle \bar{q}q \rangle(2 \text{ GeV}) = m_q(2 \text{ GeV})/m_q(1 \text{ GeV}) = 0.73$.

⁷During the calculation of diagram (a) in Figure 1, we consider only top quark in the upper loop and ignore the small contributions from other fermions. Such approximation is good enough when t_{β} is not too large, for example, $\lesssim 10$.

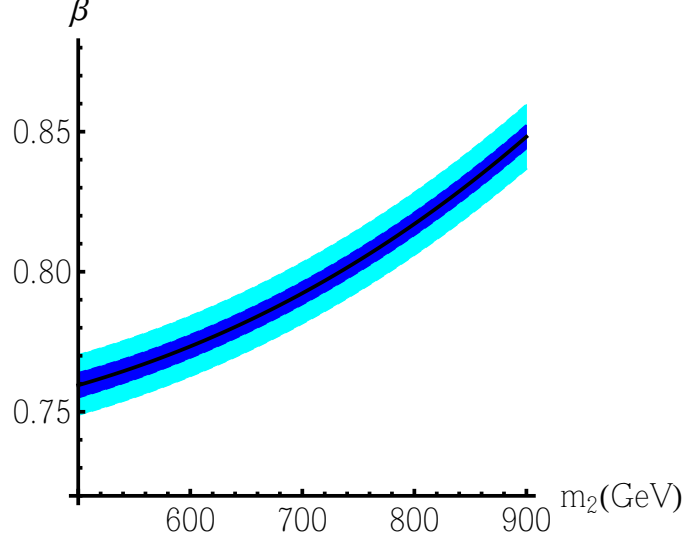
Figure 3. Cancellation behavior between β and α_1 in scenario (a) of a Type II and III 2HDM. We choose $m_2 = 500$ GeV, $m_{\pm} = 600$ GeV and $\alpha_3 = 0.8$ as an example. In both plots, the solid lines are the boundaries with $|d_e| = 1.1 \times 10^{-29} e \cdot \text{cm}$ and the regions between solid lines are allowed by the ACME experiment while the dashed lines mean $d_e = 0$. In the left plot, we choose a Type II model. The blue, orange, and red lines are shown for $\alpha_2 = 0.05, 0.1, 0.15$, respectively. In the right plot, we fix $\alpha_2 = 0.1$ and show the comparison between the Type II and Type III models. The orange lines are for the Type II model while the cyan lines are for the Type III model.



We first consider Scenario (a). For Type II and III, we show the cancellation behavior of the electron EDM in [Figure 3](#). In this scenario, the cancellation behavior is not sensitive to α_3 in a wide region (for example, $0.2 \lesssim \alpha_3 \lesssim 1.4$). Thus, we choose $\alpha_3 = 0.8$ as an example and show the cancellation behavior in the β - α_1 plane. The electron EDM sets a strict constraint which behaves as a strong correlation between β and α_1 . Numerical analysis shows that, with fixed heavy scalar masses, the location where the cancellation happens is not sensitive to α_2 , but the width of the allowed region is almost proportional to $1/s_{2\alpha_2}$. We show this behavior for the Type II model in the left plot of [Figure 3](#), for $\alpha_2 = 0.05, 0.1, 0.15$, using blue, orange and red lines, respectively. The cancellation behavior in the Type III model is similar to that in the Type II model, because the Barr-Zee diagram with a bottom quark loop is negligible and thus the only difference comes from the electron-nucleon interaction part. In the right plot of [Figure 3](#), with fixed $\alpha_2 = 0.1$, we show the comparison results between the Type II model (orange lines) and Type III model (cyan lines), finding that they are almost the same. When $m_{2,3}$ increases, the location where the cancellation happens will also change slowly and we show the corresponding results in [Figure 4](#). When m_2 increases from 500 GeV to 900 GeV, the cancellation location also moves slowly from about $\beta \simeq 0.76$ to $\beta \simeq 0.84$. The width of the allowed region is almost independent of the heavy scalar masses, as it is sensitive only to α_2 . The cancellation behavior leads to the conclusion that there is always a narrow region which is allowed by the electron EDM measurement, thus we cannot set a definite constraint on the CP-violation mixing angle α_2 only through the electron EDM, such as in the ACME experiment.

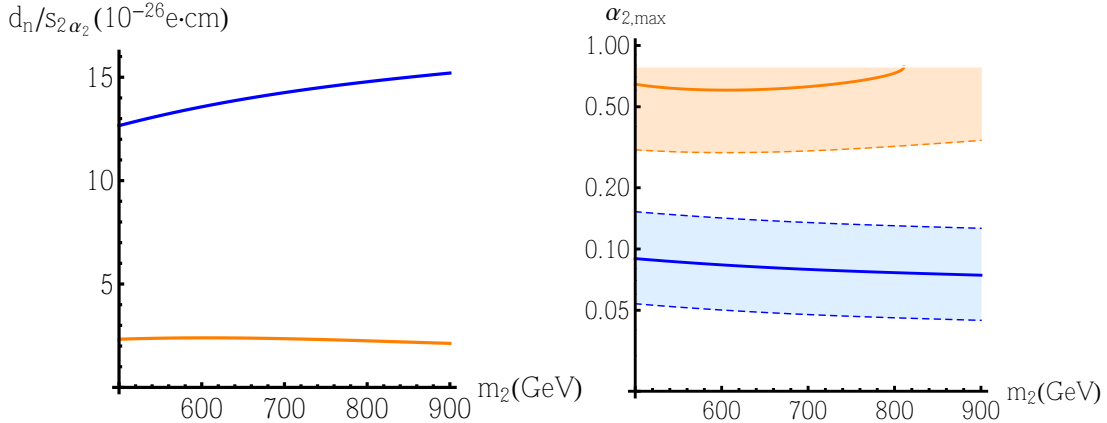
In contrast, the neutron EDM calculation does not involve such a cancellation behavior in the same region as the electron one, thus it can be used to set direct constraints on the CP-

Figure 4. Mass dependence in the cancellation region in the Type II model. Choosing $m_{\pm} - m_2 = 100$ GeV, $\alpha_3 = 0.8$, $\alpha_2 = 0.1$ and $\alpha_1 = 0$ as an example, the black line shows the value of β satisfying $d_e = 0$ while the dark blue region satisfies $|d_e| < 1.1 \times 10^{-29} e \cdot \text{cm}$, which is allowed by the ACME experiment at 90% C.L. If we set $|\alpha_1| < 0.1$, the light blue region is allowed. Results in the Type III model are almost the same and thus we do not show these.



violating mixing angle α_2 . In the parameter region allowed by the electron EDM constraints, the CEDM of the d quark contributes dominantly to the neutron EDM. Numerical analysis shows that the neutron EDM $d_n \propto s_{2\alpha_2}$ and it is not sensitive to $\alpha_{1,3}$. We calculate its

Figure 5. In the left plot, we show the $d_n/s_{2\alpha_2}$ dependence on m_2 in the Type II (blue) and Type III (orange) models using the central value estimation of Equation 3.32 in the parameter region allowed by ACME experiment. We choose $\alpha_1 = 0$ and $\alpha_3 = 0.8$ as an example, but the modification due to these two angles is less than percent level, which is far smaller than the uncertainty in the theoretical estimation (about 50% level). In the right plot, we show the limit on α_2 in the Type II (blue) and III (orange) models. The solid lines are obtained through the estimation of central value and the dashed lines are the boundaries considering the theoretical uncertainty. If theoretical uncertainties are taken into account, we cannot set any limit on α_2 in the Type III model through neutron EDM measurements.



dependence on m_2 in the Type II and III models using the central value estimated in Equation 3.32 and show the results in the left plot of Figure 5. In the Type II model, α_2 is constrained by the neutron EDM (the latest result is $|d_n| < 2.2 \times 10^{-26} e \cdot \text{cm}$ at 95% C.L. [17]). Using the central value estimation in Equation 3.32, $|\alpha_2| \lesssim (0.073 - 0.088)$ if m_2 changes in the range (500–900) GeV, as shown in the right plot of Figure 5. Considering the uncertainty in the neutron EDM estimation [88], a larger $|\alpha_2| \sim 0.15$ can also be allowed. Here, we do not consider the region α_2 close to $\pi/2$ since it corresponds to the case in which H_1 is pseudoscalar component dominated, which can be excluded by other experiments, see the next section. In the Type III model, there is almost no constraint on α_2 from the neutron EDM⁸, because there is an accidental (partial) cancellation between the two terms (see Equation 3.26) in the d quark CEDM contribution, which dominates the neutron EDM calculation.

Next, we discuss Scenario (b), in which a large mass splitting exists in $m_{2,3}$, corresponding to the cases in which α_3 is close to either $\pi/2$ or 0. From Equation 2.9, we can find two solutions for t_{α_3} as

$$t_{\alpha_3^\pm} = \frac{(m_3^2 - m_2^2) \pm \sqrt{(m_3^2 - m_2^2)^2 s_{2\beta+\alpha_1}^2 - 4(m_3^2 - m_1^2)(m_2^2 - m_1^2) s_{\alpha_2}^2 c_{2\beta+\alpha_1}^2}}{2(m_2^2 - m_1^2) s_{\alpha_2} c_{2\beta+\alpha_1}}. \quad (3.34)$$

In the large mass splitting scenario, α_3^+ is close to $\pi/2$, and α_3^- is close to 0. We choose as an example $m_2 = 500$ GeV, $m_3 = 650$ GeV and $m_\pm = 700$ GeV. In the α_3^+ case, H_2 is a CP-mixed state in which the pseudoscalar component is dominant, while H_3 is almost a pure scalar. Conversely, in the α_3^- case, H_3 is a CP-mixed state while H_2 is almost a pure scalar. In this scenario, the large mass splitting between $H_{2,3}$ leads to a significant $H_3 \rightarrow H_2 Z$ decay, because the coupling is just $c_{V,1}$, which is not suppressed by mixing angles. Numerical analysis shows a similar cancellation behavior as Scenario (a) in both α_3^\pm cases. We show the results of the Type II model in the upper two plots in Figure 6. Similar to Scenario (a), the cancellation behavior in the Type III model is almost the same as that in the Type II model and we show the comparison in the lower two plots in Figure 6.

The behavior of the neutron EDM is also similar to that of Scenario (a). In the regions allowed by electron EDM constraint, d_n is only sensitive to α_2 and is almost independent of α_1 . With the mass parameters chosen above, and using the indices II/III and $+/-$ to denote Type II/III models and $\alpha^{+/-}$ cases, we have

$$d_n^{\text{II},+}/s_{2\alpha_2} \simeq 1.4 \times 10^{-25} e \cdot \text{cm}, \quad (3.35)$$

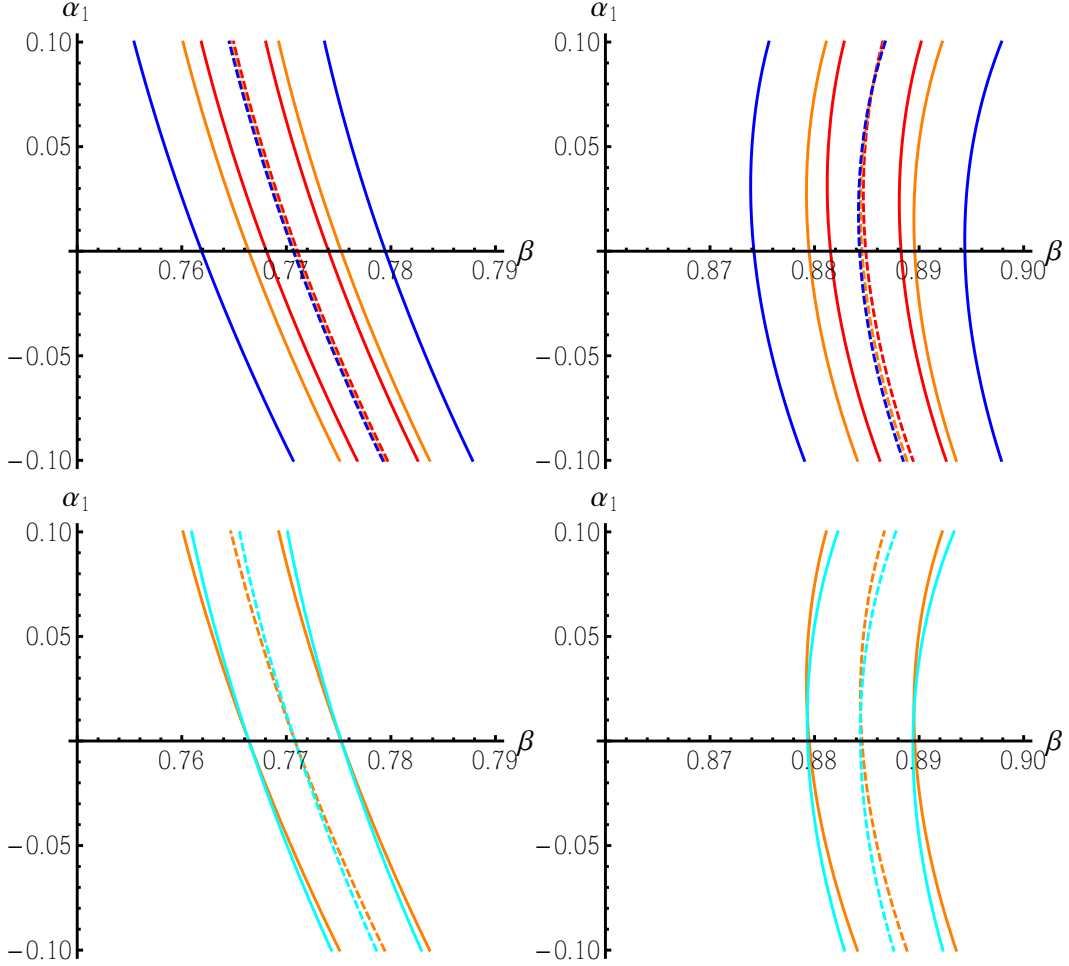
$$d_n^{\text{II},-}/s_{2\alpha_2} \simeq 1.3 \times 10^{-25} e \cdot \text{cm}, \quad (3.36)$$

$$d_n^{\text{III},+}/s_{2\alpha_2} \simeq 2.4 \times 10^{-26} e \cdot \text{cm}, \quad (3.37)$$

$$d_n^{\text{III},-}/s_{2\alpha_2} \simeq 1.9 \times 10^{-26} e \cdot \text{cm}, \quad (3.38)$$

⁸If we consider only the central value of the neutron EDM estimation Equation 3.32, the constraint is about $|s_{2\alpha_2}| \lesssim 0.9$, meaning that $\alpha_{2,\text{max}}$ is already close to $\pi/4$. However, if the large theoretical uncertainty in the neutron EDM estimation is also taken into account, we cannot exclude any value for $|s_{2\alpha_2}| \leq 1$, which means no constraint on $|\alpha_2|$ can be set in the Type III model.

Figure 6. Similar to Scenario (a), the electron EDM sets a strict constraint which behaves as a strong correlation between β and α_1 . We show the cancellation behavior of the Type II model in the upper two plots and present the comparison between the Type II and III models in the lower two plots. The notation is the same as in Figure 3. The left two plots correspond to the case α_3^+ in the allowed region $\alpha_3^+ \simeq \pi/2 - 1.5 \times 10^{-2} \alpha_2$ while the right two plots correspond to the case α_3^- in the allowed region $\alpha_3^- \simeq -0.52 \alpha_2$.



based on the central value estimation in Equation 3.32. Thus, we can obtain the upper limit on α_2 in the Type II model as

$$\alpha_2 \lesssim \begin{cases} 0.079, & (\alpha_3^+ \text{ case}), \\ 0.085, & (\alpha_3^- \text{ case}). \end{cases} \quad (3.39)$$

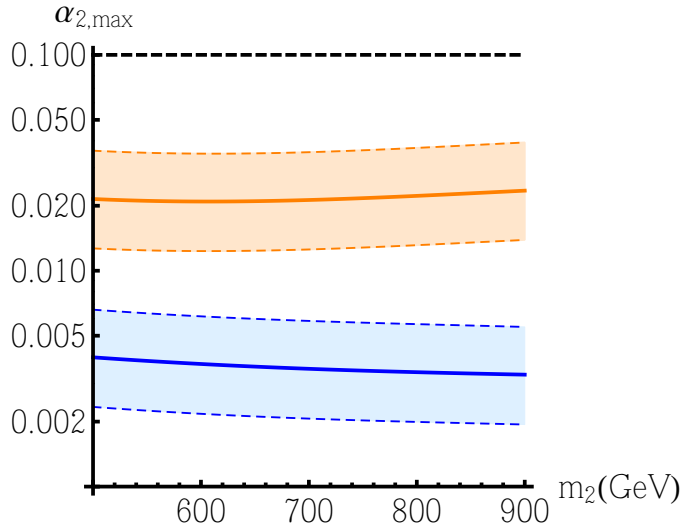
There is no constraint on α_2 from the neutron EDM in the Type III model, due to the same reason as discussed above for Scenario (a).

3.4 Future Neutron EDM Tests

Several groups are currently planning new measurements on neutron EDM, to the accuracy of $\mathcal{O}(10^{-27} e \cdot \text{cm})$ or even better [11, 13, 91–94]. Such an order of magnitude improvement

in accuracy would be very helpful to perform further tests on the 2HDM Type II and III scenarios considered here.

Figure 7. Upper limit on α_2 in the Type II and III models when the future limit decreases to $|d_n| < 10^{-27} e \cdot \text{cm}$. The color scheme is the same as above: blue for the Type II model and orange for the Type III model. The solid lines are obtained using the central value estimation and, if we consider the theoretical uncertainty estimation of [88], the boundaries of the limits on α_2 are the dashed lines.



If no anomaly is discovered in future neutron EDM measurements, the upper limit on d_n would improve to about $10^{-27} e \cdot \text{cm}$, and there would be more stringent limits on α_2 in both Type II and III models, as shown in Figure 7 for Scenario (a). Further, α_2 can be constrained to $\mathcal{O}(10^{-2})$ in the Type III model and to $\mathcal{O}(10^{-3})$ in Type II model. Similar constraints can be placed in Scenario (b). In contrast, if $\alpha_2 \sim \mathcal{O}(0.1)$, there will be significant BSM evidence in future neutron EDM measurements. In the models which contain a similar cancellation mechanism in electron EDM, the neutron EDM experiments may be used to find the first evidence of CP-violation or set the strictest limit directly on the CP-violating phase α_2 .

3.5 Summary on EDM Tests

In the previous subsections, we have discussed the electron and neutron EDM tests in the 2HDM with soft CP-violation. There is no cancellation mechanism in the Type I and IV models and thus the electron EDM can set strict constraints on the CP-violation angle as $\arg(c_{f,1}) \simeq s_{\alpha_2}/t_\beta \lesssim 8.5 \times 10^{-4}$. However, this value is too small to give any observable CP effects in other experiments, thus we decided not to have further discussions on these two 2HDM realizations. In contrast, cancellations among various contributions to the electron EDM can occur in the Type II and III models. Here, we still face stringent constraints but these will induce a strong correlation between β and α_1 . We cannot set constraints directly on the CP-violation mixing angle α_2 though. The behavior is the same in the Type II and III models. In fact, it is also the same in both Scenario (a), in which $m_{2,3}$ are close to

each other, and in Scenario (b), in which $m_{2,3}$ have large splitting. A cancellation generally happens around $t_\beta \sim 1$ with the exact location depending weakly on the masses of the heavy (pseudo)scalars.

Current measurements of the neutron EDM can set an upper limit on $|\alpha_2| \simeq (0.073 - 0.088)$ in the Type II model, depending on different scenarios and masses, if we take the central value of the neutron EDM estimation. Such limits can be weakened to about 0.15 if we consider the theoretical uncertainty. But one cannot set limits on α_2 in the Type III model, because the CEDM of the d quark in this model is suppressed by a partial cancellation. However, α_2 in the Type III model is constrained by collider tests, which will be discussed in the next section.

Finally, we showed the importance of future neutron EDM measurements in our models relying on the cancellation mechanism in the electron EDM. For $\alpha_2 \sim \mathcal{O}(0.1)$, there would be significant evidence in future neutron EDM experiments, which will be more sensitive than any other experiments. And if there is no evidence of non-zero neutron EDM, the improved limit on the neutron EDM will set strict constraints on the CP-violation mixing angle: the upper limit of $|\alpha_2|$ will reach $\mathcal{O}(10^{-2})$ in the Type III model and $\mathcal{O}(10^{-3})$ in the Type II model.

4 Current Collider Constraints

Any BSM model must face LHC tests. In our 2HDM with soft CP-violation, as mentioned, we treat H_1 as the 125 GeV Higgs boson. In this scenario then, the latter mixes with the other (pseudo)scalar states and its couplings will be modified from the corresponding SM values. However, these modified couplings are constrained by global fits on the so-called Higgs signal-strength measurements. In addition, the scalar sector is extended in a 2HDM, so that direct searches for these new particles at the LHC will also set further constraints on this BSM scenario. In this respect, we discuss only the 2HDM Type II and III, in which the cancellation behavior in the electron EDM requires t_β close to 1.

4.1 Global Fit on Higgs Signal Strengths

The Higgs boson H_1 can be mainly produced at the LHC through four channels: gluon fusion (ggF), vector boson fusion (VBF), associated production with vector boson ($V + H_1$, here $V = W, Z$) or a top quark pair ($t\bar{t} + H_1$) [95–98]. The decay channels $H \rightarrow b\bar{b}, \tau^+\tau^-, \gamma\gamma, WW^*$ and ZZ^* have already been discovered. Define the signal strength $\mu_{i,f}$ corresponding to production channel i and decay channel f as follows:

$$\mu_{i,f} \equiv \frac{\sigma_i}{\sigma_{i,\text{SM}}} \cdot \frac{\Gamma_f}{\Gamma_{f,\text{SM}}} \cdot \frac{\Gamma_{\text{tot,SM}}}{\Gamma_{\text{tot}}}, \quad (4.1)$$

where σ_i denotes the production cross section of the production channel i amongst those listed above, Γ_f denotes the decay width of channel f and Γ_{tot} denotes the total decay width of H_1 . A quantity with index “SM” denotes the value predicted by the SM. Such signal strengths for different channels have been measured by the ATLAS [99–102] and CMS [103–105] collaborations: we list them in Table 3.

Table 3. Signal strengths measurements by the ATLAS (top) and CMS (bottom) collaborations at $\sqrt{s} = 13$ TeV. The luminosity is $\leq 139 \text{ fb}^{-1}$ for the ATLAS measurements and $\leq 137 \text{ fb}^{-1}$ for the CMS measurements.

	ggF	VBF	$V + H$	$t\bar{t} + H$
$H \rightarrow b\bar{b}$	-	$3.01^{+1.67}_{-1.61}$	$1.19^{+0.27}_{-0.25}$	$0.79^{+0.60}_{-0.59}$
$H \rightarrow \tau^+\tau^-$	$0.96^{+0.59}_{-0.52}$	$1.16^{+0.58}_{-0.53}$	-	$1.38^{+1.13}_{-0.96}$
$H \rightarrow \gamma\gamma$	$0.96^{+0.14}_{-0.14}$	$1.39^{+0.40}_{-0.35}$	$1.09^{+0.58}_{-0.54}$	$1.38^{+0.32}_{-0.30}$
$H \rightarrow WW^*$	$1.08^{+0.19}_{-0.19}$	$0.59^{+0.36}_{-0.35}$	-	$1.56^{+0.42}_{-0.40}$
$H \rightarrow ZZ^*$	$1.04^{+0.16}_{-0.15}$	$2.68^{+0.98}_{-0.83}$	$0.68^{+1.20}_{-0.78}$	-
	ggF	VBF	$V + H$	$t\bar{t} + H$
$H \rightarrow b\bar{b}$	$2.45^{+2.53}_{-2.35}$	-	$1.06^{+0.26}_{-0.25}$	$1.13^{+0.33}_{-0.30}$
$H \rightarrow \tau^+\tau^-$	$0.39^{+0.38}_{-0.39}$	$1.05^{+0.30}_{-0.29}$	$2.2^{+1.1}_{-1.0}$	$0.81^{+0.74}_{-0.67}$
$H \rightarrow \gamma\gamma$	$1.09^{+0.15}_{-0.14}$	$0.77^{+0.37}_{-0.29}$	-	$1.62^{+0.52}_{-0.43}$
$H \rightarrow WW^*$	$1.28^{+0.20}_{-0.19}$	$0.63^{+0.65}_{-0.61}$	$1.64^{+1.36}_{-1.14}$	$0.93^{+0.48}_{-0.45}$
$H \rightarrow ZZ^*$	$0.98^{+0.12}_{-0.11}$	$0.57^{+0.46}_{-0.36}$	$1.10^{+0.96}_{-0.74}$	$0.25^{+1.03}_{-0.25}$

As intimated, in the 2HDM, H_1 couplings to SM particles are modified due to the mixing with other (pseudo)scalars and thus the aforementioned signal strengths are modified. The production cross sections satisfy [106–108]

$$\frac{\sigma_{\text{VBF}}}{\sigma_{\text{VBF,SM}}} = \frac{\sigma_{V+H}}{\sigma_{V+H,SM}} = c_{V,1}^2, \quad (4.2)$$

$$\frac{\sigma_{ggF}}{\sigma_{ggF,SM}} = \left| \text{Re}(c_{t,1}) + i \frac{\mathcal{B}_1\left(\frac{z_{H_1 t}}{4}\right)}{\mathcal{A}_1\left(\frac{z_{H_1 t}}{4}\right)} \text{Im}(c_{t,1}) \right|^2 \simeq [\text{Re}(c_{t,1})]^2 + 2.3 [\text{Im}(c_{t,1})]^2, \quad (4.3)$$

$$\frac{\sigma_{t\bar{t}+H}}{\sigma_{t\bar{t}+H,SM}} \simeq [\text{Re}(c_{t,1})]^2 + 0.37 [\text{Im}(c_{t,1})]^2, \quad (4.4)$$

while the decay widths satisfy [106, 107]

$$\frac{\Gamma_{ZZ^*}}{\Gamma_{ZZ^*,SM}} = \frac{\Gamma_{WW^*}}{\Gamma_{WW^*,SM}} = c_{V,1}^2, \quad (4.5)$$

$$\frac{\Gamma_{f\bar{f}}}{\Gamma_{f\bar{f},SM}} = |c_{f,1}|^2, \quad (f = c, b, \tau), \quad (4.6)$$

$$\frac{\Gamma_{gg}}{\Gamma_{gg,SM}} = \left| \text{Re}(c_{t,1}) + i \frac{\mathcal{B}_1\left(\frac{z_{H_1 t}}{4}\right)}{\mathcal{A}_1\left(\frac{z_{H_1 t}}{4}\right)} \text{Im}(c_{t,1}) \right|^2 \simeq [\text{Re}(c_{t,1})]^2 + 2.3 [\text{Im}(c_{t,1})]^2, \quad (4.7)$$

$$\begin{aligned} \frac{\Gamma_{\gamma\gamma}}{\Gamma_{\gamma\gamma,SM}} &= \left| \frac{\frac{c_{\pm,1} v^2}{2m_{\pm}^2} \mathcal{A}_0\left(\frac{z_{1,\pm}}{4}\right) + c_{V,1} \mathcal{A}_2\left(\frac{z_{H_1 W}}{4}\right) + \frac{4}{3} [\text{Re}(c_{t,1}) \mathcal{A}_1\left(\frac{z_{H_1 t}}{4}\right) + i \text{Im}(c_{t,1}) \mathcal{B}_1\left(\frac{z_{H_1 t}}{4}\right)]}{\frac{4}{3} \mathcal{A}_1\left(\frac{z_{H_1 t}}{4}\right) + \mathcal{A}_2\left(\frac{z_{H_1 W}}{4}\right)} \right|^2 \\ &\simeq [1.28 c_{V,1} - 0.28 \text{Re}(c_{t,1}) - 0.02]^2 + 0.19 [\text{Im}(c_{t,1})]^2. \end{aligned} \quad (4.8)$$

The loop functions $\mathcal{A}_{0,1,2}$ and \mathcal{B}_1 are listed in Appendix D. Here, $c_{V,1} = c_{\alpha_1} c_{\alpha_2}$ holds for all types of models, while $c_{f,1}$ which depends on the model type are listed in Appendix A.

The $t\bar{t} + H_1$ cross section ratio in Equation 4.4 is only valid for the LHC at $\sqrt{s} = 13$ TeV. For the $\gamma\gamma$ decay Equation 4.8, the charged Higgs loop contribution is small compared with the top quark and W loops, and we choose the case $m_{\pm} = 600$ GeV for illustration. The total width satisfies

$$\frac{\Gamma_{\text{tot}}}{\Gamma_{\text{tot,SM}}} = \sum_f \text{BR}_f^{\text{SM}} \cdot \frac{\Gamma_f}{\Gamma_{f,\text{SM}}}. \quad (4.9)$$

BR_f^{SM} is the SM prediction on the Branching Ratio (BR) of the SM Higgs boson decay to the final state f , thus all the modifications are normalized to the SM values. For the 125 GeV SM Higgs boson, we list the theoretical predictions on the BRs of the main decay channels in Table 4 [98].

Table 4. Predictions of the main BRs of the SM Higgs boson with mass 125 GeV.

$\text{BR}_{b\bar{b}}^{\text{SM}}$	$\text{BR}_{\tau^+\tau^-}^{\text{SM}}$	$\text{BR}_{c\bar{c}}^{\text{SM}}$	$\text{BR}_{WW^*}^{\text{SM}}$	$\text{BR}_{ZZ^*}^{\text{SM}}$	$\text{BR}_{gg}^{\text{SM}}$
58.2%	6.3%	2.9%	21.4%	2.6%	8.2%

We perform χ^2 -fits where

$$\chi^2 \equiv \sum_{i,f} \left(\frac{\mu_{i,f}^{\text{exp}} - \mu_{i,f}^{\text{th}}}{\delta\mu_{i,f}^2} \right)^2, \quad (4.10)$$

where $\mu_{i,f}^{\text{th}}$ is the theoretically predicted signal strength, $\mu_{i,f}^{\text{exp}}$ is the experimentally measured one and $\delta\mu_{i,f}$ is the associated uncertainty. The possible small correlations across production and decay channels are ignored. For a 2HDM, χ^2 depends only on $\beta, \alpha_{1,2}$. We perform global fits for the Type II and III models, in which $\alpha_2 \sim \mathcal{O}(0.1)$ is still allowed. The minimal χ^2 (denoted by χ_{min}^2) obtained from ATLAS and CMS data as well as the combined one are listed in Table 5. The fitting, normalized to the degrees of freedom

Table 5. The $\chi_{\text{min}}^2/\text{d.o.f.}$ for the Type II and Type III models using ATLAS data, CMS data and their combination, respectively.

$\chi_{\text{min}}^2/\text{d.o.f.}$	ATLAS	CMS	ATLAS+CMS
Type II	11.8/13	12.2/15	24.2/31
Type III	12.7/13	11.9/15	24.8/31

(d.o.f.), is good enough because the models approach the SM limit when $\alpha_{1,2} \rightarrow 0$. If one then defines $\delta\chi^2 \equiv \chi^2 - \chi_{\text{min}}^2$, this is useful to find the allowed parameter regions of the two 2HDM realizations considered. Our numerical study shows that the results depend weakly on β . We choose $\beta = 0.76$ (corresponding to $m_{2,3} \sim 500$ GeV in Scenario (a)) as an example and show the allowed region from combined ATLAS and CMS results in the $\alpha_2 - \alpha_1$ plane in Figure 8. For both Type II and III, the global fit requires $|\alpha_2| \lesssim 0.33$ in the region $\beta \sim (0.7 - 1)$. For the Type II model, this constraint is weaker when compared with that from the neutron EDM. Nevertheless, it can set a new constraint on $|\alpha_2|$ for the Type III model. The allowed range for $|\alpha_1|$ in the latter is wider than the one in the Type

Figure 8. Allowed regions in the $\alpha_2 - \alpha_1$ plane obtained by using the combined results from the ATLAS and CMS collaborations, with fixed $\beta = 0.76$ for Type II (left) and Type III (right). Green regions are allowed at 68% C.L. ($\delta\chi^2 \leq 2.3$) and yellow regions are allowed at 95% C.L. ($\delta\chi^2 \leq 6.0$).

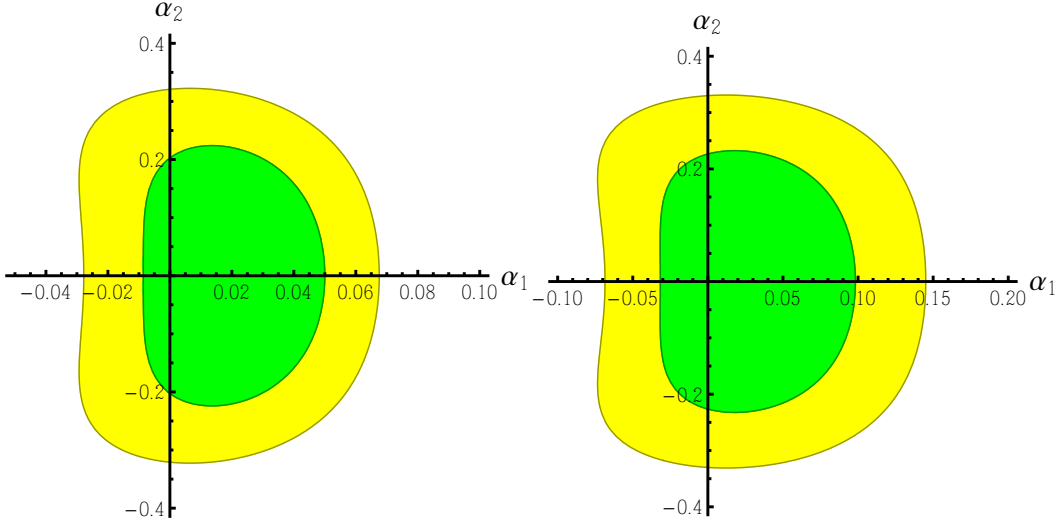
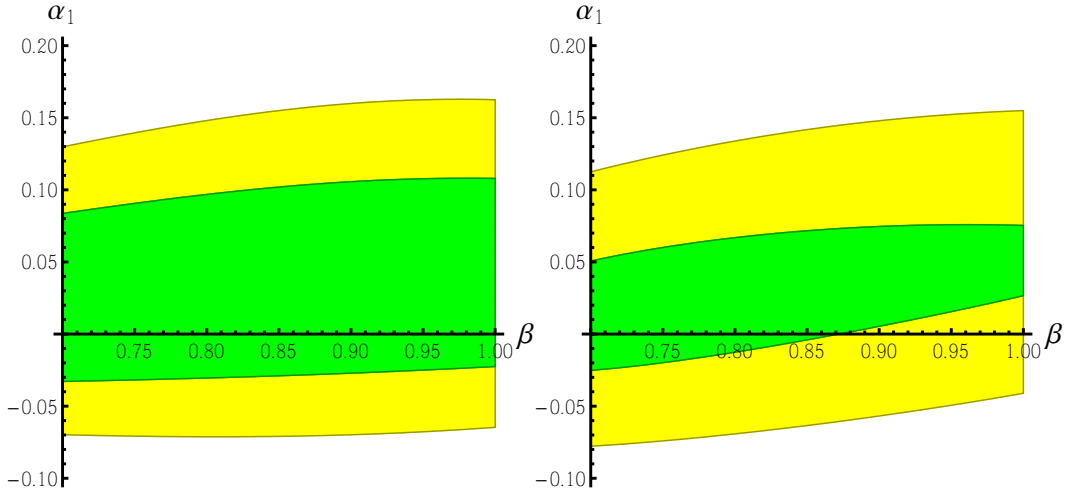


Figure 9. Allowed regions in the $\alpha_1 - \beta$ plane obtained by using the combined results from the ATLAS and CMS collaborations, with fixed $\alpha_2 = 0.1$ (left) and 0.2 (right), in the Type III model. Green regions are allowed at 68% C.L. ($\delta\chi^2 \leq 2.3$) and yellow regions are allowed at 95% C.L. ($\delta\chi^2 \leq 6.0$).



II model, in fact. In both models, α_1 is favored when close to 0, thus, in the following discussion, we usually fix $\alpha_1 = 0.02$, a value which is not far from the best fit points in most cases. In [Figure 9](#), we show instead the allowed regions in the $\alpha_1 - \beta$ plane for fixed $\alpha_2 = 0.1, 0.2$ in the Type III model. The dependence on β is indeed weak, but it increases somewhat when α_2 gets larger, as shown in the figure.

4.2 LHC Direct Searches for Heavy Scalars

In the 2HDM, there are four additional scalars, $H_{2,3}$ and H^\pm , beyond the SM-like one H_1 . Thus, we must also check the direct searches for these (pseudo)scalars at the LHC. Notice that $H_{2,3}$ decay to $t\bar{t}$ dominantly and we show their decay widths and BRs in [Appendix E](#). The $H_{2,3} \rightarrow 2H_1$ decays are ignored because such channels are suppressed in the allowed parameter region isolated so far. In Scenario (b), $H_3 \rightarrow ZH_2$ decay is also open if $m_3 - m_2 > m_Z$. In addition, H^- decays to $t\bar{b}$ dominantly.

We first consider the process $gg \rightarrow H_{2,3} \rightarrow ZZ$. Theoretically, this process is sensitive to the couplings between $H_{2,3}$ and the gauge vector bosons, hence sensitive to α_2 . Experimentally, this process is the most sensitive channel in searching for heavy neutral scalars. The current LHC limit for $m_2 = 500$ GeV is $\sigma_{gg \rightarrow H_{2,3} \rightarrow ZZ} \lesssim 0.1$ pb at 95% C.L. [109] at $\sqrt{s} = 13$ TeV with about 40 fb^{-1} of luminosity. In such processes, our numerical study shows that the interference between $H_{2,3}$ production and the SM background is small, thus we can safely consider only the resonant production. However, for Scenario (a), in which $H_{2,3}$ are close in mass such that $|m_2 - m_3| \simeq \mathcal{O}(\text{GeV}) \ll \Gamma_{2,3} \simeq 20$ GeV for $m_2 \simeq 500$ GeV (where we have denoted by $\Gamma_{2,3}$ the widths of the two heavy Higgs states), we must consider the interference between the H_2 and H_3 production processes. To the one-loop order, we have

$$\sigma_{gg \rightarrow H_{2,3} \rightarrow ZZ} = \sigma_S + \sigma_P, \quad (4.11)$$

where σ_S is the contribution from $\text{Re}(c_{t,2,3})$ and σ_P is the contribution from $\text{Im}(c_{t,2,3})$. Their ZZ invariant mass distributions are then separately given by

$$\begin{aligned} \frac{d\sigma_S}{dq} &= \int dx_1 dx_2 f_g(x_1) f_g(x_2) \delta\left(x_1 x_2 - \frac{q^2}{s}\right) \hat{\sigma}_S(q) \\ &\quad \times \frac{2q^3 m_2 \Gamma_0(q)}{\pi s} \left| \sum_{i=2,3} \frac{c_{V,i} \text{Re}(c_{t,i})}{q^2 - m_i^2 - im_i \Gamma_i} \right|^2, \end{aligned} \quad (4.12)$$

$$\begin{aligned} \frac{d\sigma_P}{dq} &= \int dx_1 dx_2 f_g(x_1) f_g(x_2) \delta\left(x_1 x_2 - \frac{q^2}{s}\right) \hat{\sigma}_P(q) \\ &\quad \times \frac{2q^3 m_2 \Gamma_0(q)}{\pi s} \left| \sum_{i=2,3} \frac{c_{V,i} \text{Im}(c_{t,i})}{q^2 - m_i^2 - im_i \Gamma_i} \right|^2. \end{aligned} \quad (4.13)$$

In the equations above, $f_g(x)$ denotes the gluon Parton Distribution Function (PDF), which, in our numerical study, is chosen to be the MSTW2008 set [110]. The function [106, 107]

$$\Gamma_0(q) = \frac{q^3 \alpha_{\text{em}}}{32 s_{2\theta_W}^2 m_Z^2} \left(1 - \frac{4m_Z^2}{q^2}\right) \left(1 - \frac{4m_Z^2}{q^2} + \frac{12m_Z^4}{q^4}\right), \quad (4.14)$$

is the decay width to the ZZ final state of a would-be SM Higgs boson with mass q . The

functions [106, 107]

$$\hat{\sigma}_S(q) = \frac{G_F \alpha_s^2}{288 \sqrt{2} \pi} \left| \frac{3}{4} \mathcal{A}_1 \left(\frac{q^2}{4m_t^2} \right) \right|, \quad (4.15)$$

$$\hat{\sigma}_P(q) = \frac{G_F \alpha_s^2}{288 \sqrt{2} \pi} \left| \frac{3}{4} \mathcal{B}_1 \left(\frac{q^2}{4m_t^2} \right) \right| \quad (4.16)$$

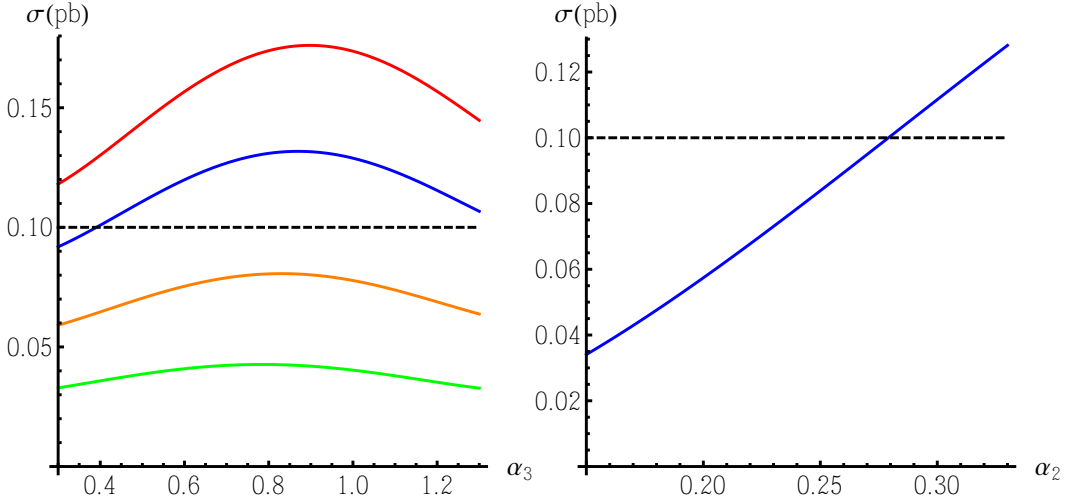
are the parton-level cross sections of a pure scalar(pseudoscalar) state with couplings $c_t = 1(i)$. The loop functions \mathcal{A}_1 and \mathcal{B}_1 are listed in Appendix D. Thus, the total cross section is

$$\sigma_{gg \rightarrow H_{2,3} \rightarrow ZZ} = \int_{m_{2,3} - \Delta q/2}^{m_{2,3} + \Delta q/2} dq \left(\frac{d\sigma_S}{dq} + \frac{d\sigma_P}{dq} \right). \quad (4.17)$$

For $m_2 \simeq 500$ GeV, we choose $\Delta q = 50$ GeV as the mass window where interference is accounted for.

Numerically, we show the cross sections depending on the mixing angles in Figure 10 by fixing $m_2 = 500$ GeV in the Type III model. The left plot is for Scenario (a) and the

Figure 10. Cross sections $\sigma_{gg \rightarrow H_{2,3} \rightarrow ZZ}$ as a function of the mixing angles $\alpha_{2,3}$ in the Type III model. In the left plot, we show the cross section depending on α_3 in Scenario (a), fixing $\beta = 0.76$ and $\alpha_1 = 0.02$. From top to bottom, the four lines show results with $\alpha_2 = 0.33, 0.27, 0.2, 0.14$, respectively. In the right plot, we show the cross section depending on α_2 in Scenario (b), fixing $\beta = 0.76$ and $\alpha_1 = 0.02$, with α_3 chosen as $\alpha_3^+ (\simeq 1.5 \times 10^{-2} \alpha_2)$ which corresponds to $m_3 \simeq 650$ GeV.



right plot is for Scenario (b) for the α_3^+ case. In both scenarios, we can see that $\alpha_2 \lesssim 0.27$ is favored when $m_2 = 500$ GeV. Thus, in the following analysis, we generally choose $\alpha_2 = 0.27$ (unless stated otherwise) as a benchmark point, corresponding to the largest allowed CP-violation effects. For Scenario (a), when we choose $\alpha_2 = 0.27$, $\alpha_3 \lesssim 0.4$ or $\gtrsim 1.2$ is favored, which still keeps $H_{2,3}$ nearly degenerate in mass. For Scenario (b) and the α_3^- case, $c_{2,V}$ is suppressed (close to α_1), thus it faces no further constraints here. In the Type II model, we can obtain the same cross section as that in the Type III model with the same parameters.

In the Type II model, due to the stricter neutron EDM constraint, the considered parameter space is always allowed.

As mentioned, $H_{2,3}$ decay dominantly to a $t\bar{t}$ final state and the current LHC limit for $m_2 = 500$ GeV is about $\sigma_{pp \rightarrow H_{2,3} \rightarrow t\bar{t}} \lesssim 7$ pb at 95% C.L. [111] at $\sqrt{s} = 13$ TeV and 36 fb^{-1} of luminosity. In contrast to the ZZ channel, the interference with SM background is very important in the $t\bar{t}$ channel [112, 113], which strongly decreases the signal cross section compared with the pure resonance production cross section, so long that non-resonant Higgs diagrams can be subtracted [?]. The total cross section can be divided into

$$\sigma_{gg \rightarrow t\bar{t}} = \sigma_{\text{SM}} + \sigma_{\text{res}} + \sigma_{\text{int}} = \sigma_{\text{SM}} + \delta\sigma_{t\bar{t}}. \quad (4.18)$$

Here, σ_{SM} denotes the SM cross section while σ_{res} and σ_{int} denote the resonant and interference cross section, separately. Furthermore, $\delta\sigma_{t\bar{t}}$ is the cross section difference between 2HDM and SM, i.e.,

$$\delta\sigma_{t\bar{t}} \equiv \sigma_{\text{res}} + \sigma_{\text{int}} = \int dx_1 dx_2 f_g(x_1) f_g(x_2) (\hat{\sigma}_{\text{res}} + \hat{\sigma}_{\text{int}}), \quad (4.19)$$

where $\hat{\sigma}$ denotes the parton-level cross section as a function of the $t\bar{t}$ invariant mass q . Following the results in [112, 113], we have

$$\begin{aligned} \hat{\sigma}_{\text{res}} &= \hat{\sigma}_{\text{res},S} + \hat{\sigma}_{\text{res},P} \\ &= \frac{3\alpha_s^2 G_F^2 m_t^2 q^4}{4096\pi^3} \left[\beta_t^3 \left(\left| \sum_{i=2,3} \frac{[\text{Re}(c_{t,i})]^2 \mathcal{A}_1\left(\frac{q^2}{4m_t^2}\right)}{q^2 - m_i^2 - im_i\Gamma_i} \right|^2 + \left| \sum_{i=2,3} \frac{[\text{Re}(c_{t,i})\text{Im}(c_{t,i})] \mathcal{B}_1\left(\frac{q^2}{4m_t^2}\right)}{q^2 - m_i^2 - im_i\Gamma_i} \right|^2 \right) \right. \\ &\quad \left. + \beta_t \left(\left| \sum_{i=2,3} \frac{[\text{Re}(c_{t,i})\text{Im}(c_{t,i})] \mathcal{A}_1\left(\frac{q^2}{4m_t^2}\right)}{q^2 - m_i^2 - im_i\Gamma_i} \right|^2 + \left| \sum_{i=2,3} \frac{[\text{Im}(c_{t,i})]^2 \mathcal{B}_1\left(\frac{q^2}{4m_t^2}\right)}{q^2 - m_i^2 - im_i\Gamma_i} \right|^2 \right) \right], \quad (4.20) \end{aligned}$$

$$\begin{aligned} \hat{\sigma}_{\text{int}} &= \hat{\sigma}_{\text{int},S} + \hat{\sigma}_{\text{int},P} \\ &= - \int_{-1}^1 dc_\theta \frac{\alpha_s G_F m_t^2}{64\sqrt{2}\pi(1 - \beta_t^2 c_\theta^2)} \\ &\quad \times \text{Re} \left[\beta_t^3 \sum_{i=2,3} \frac{[\text{Re}(c_{t,i})]^2 \mathcal{A}_1\left(\frac{q^2}{4m_t^2}\right)}{q^2 - m_i^2 - im_i\Gamma_i} + \beta_t \sum_{i=2,3} \frac{[\text{Im}(c_{t,i})]^2 \mathcal{B}_1\left(\frac{q^2}{4m_t^2}\right)}{q^2 - m_i^2 - im_i\Gamma_i} \right]. \quad (4.21) \end{aligned}$$

Here, $q^2 = x_1 x_2 s$, $\beta_t = \sqrt{1 - 4m_t^2/q^2}$ is the velocity of the top quark in the $t\bar{t}$ center-of-mass frame. In our numerical study, we set q in the range $m_2 - \Delta'q/2 < q < m_2 + \Delta'q/2$, where we choose the mass window $\Delta'q = 100$ GeV for $m_2 = 500$ GeV. We choose the MSTW2008 PDF [110] as above. We show the cross sections for some benchmark points in both Scenario (a) and Scenario (b) in Table 6. The numerical results show that, for all benchmark points we consider, the interference with the SM background significantly breaks the resonance structure of $H_{2,3}$ and decreases the cross sections to around (even

Table 6. Cross sections $\delta\sigma_{t\bar{t}}$ at the LHC with $\sqrt{s} = 13$ TeV, fixing $m_2 = 500$ GeV and $\alpha_1 = 0.02$. Further, for the Type II model (denoted as $\delta\sigma_{t\bar{t}}^{\text{II}}$) we fix $\alpha_2 = 0.14$ while for the Type III model (denoted as $\delta\sigma_{t\bar{t}}^{\text{III}}$) we fix $\alpha_2 = 0.27$. The left table is for Scenario (a), in which we fix $\beta = 0.76$ and choose $\alpha_3 = 0.4, 0.8, 1.2$ from top to bottom. The right table is for Scenario (b), in which we fix $m_3 = 650$ GeV, considering two cases: $\beta = 0.77, \alpha_3 = \alpha_3^+$ and $\beta = 0.885, \alpha_3 = \alpha_3^-$, again, from top to bottom.

α_3	$\delta\sigma_{t\bar{t}}^{\text{II}}$ (pb)	$\delta\sigma_{t\bar{t}}^{\text{III}}$ (pb)	α_3	$\delta\sigma_{t\bar{t}}^{\text{II}}$ (pb)	$\delta\sigma_{t\bar{t}}^{\text{III}}$ (pb)
0.4	0.04	-0.40	α_3^+	-0.43	-0.67
0.8	0.39	-0.11	α_3^-	0.72	0.53
1.2	0.25	-0.07			

below) 0, which means the $t\bar{t}$ resonant search at the LHC cannot set limits on this model⁹.

The $H_{2,3}$ states can also be produced in association with a $t\bar{t}$ pair at the LHC, thus we should also check this constraint for our favored benchmark points. Since $H_{2,3}$ mainly decay into a $t\bar{t}$ pair, the whole production and decay process will modify the cross section of the $pp \rightarrow t\bar{t}t\bar{t}$ process (which we denote by σ_{4t}), which current LHC limit is about 22.5 fb at 95% C.L. [116] at $\sqrt{s} = 13$ TeV with 137 fb^{-1} of integrated luminosity. The interference effects between SM and BSM contributions are expected to be significant [117]. We estimate this cross section in the 2HDM considering all interference effects by using MADGRAPH5_AMC@NLO [118, 119]. We then show the numerical results in Table 7 for some benchmark points, all allowed by current LHC limits.

Table 7. Cross sections σ_{4t} at the LHC with $\sqrt{s} = 13$ TeV, fixing $m_2 = 500$ GeV and $\alpha_1 = 0.02$. Further, for the Type II model (denoted as σ_{4t}^{II}) we fix $\alpha_2 = 0.14$ while for the Type III model (denoted as σ_{4t}^{III}) we fix $\alpha_2 = 0.27$. The left table is for Scenario (a), in which we fix $\beta = 0.76$ and choose $\alpha_3 = 0.4, 0.8, 1.2$ from top to bottom. The right table is for Scenario (b), in which we fix $m_3 = 650$ GeV, considering two cases: $\beta = 0.77, \alpha_3 = \alpha_3^+$ and $\beta = 0.885, \alpha_3 = \alpha_3^-$, again, from top to bottom.

α_3	σ_{4t}^{II} (fb)	σ_{4t}^{III} (fb)	α_3	σ_{4t}^{II} (fb)	σ_{4t}^{III} (fb)
0.4	19.9	17.9	α_3^+	15.9	14.3
0.8	20.8	18.7	α_3^-	10.4	9.4
1.2	20.8	19.3			

Finally, we should also check the direct LHC limits on the charged Higgs boson H^\pm . As mentioned above, $b \rightarrow s\gamma$ decay favors a heavy H^\pm state with mass $m_\pm \gtrsim 600$ GeV [50, 51]. For $m_\pm = 600$ GeV, the current LHC limit is about 0.1 pb at 95% C.L. [120, 121] at $\sqrt{s} = 13$ with some 36 fb^{-1} of luminosity TeV. For large t_β , the interference effect is negligible [122]. However, in the Type II and Type III models with CP-violation as considered above, $t_\beta \sim 1$ is favored. For $m_\pm \simeq 600$ GeV, its width $\Gamma_\pm \gtrsim 30$ GeV, which leads to significant interference effects. Again, we estimate the cross section considering all

⁹In some experimental analyses [114, 115], the interference effects between (pseudo)scalar resonance and the SM background were taken into account. Yet, the results cannot be simply rescaled to our CP-violating scenario, because of the existence of CP-violation will modify the shape of the $t\bar{t}$ invariant mass compared with the CP-conserving case. We still need further studies on such scenarios.

interference effects using MADGRAPH5_AMC@NLO [118, 119]. If we denote by $\delta\sigma_{\pm}$ the cross section modification (including both the resonant and interference effects) to SM $t\bar{t}b\bar{b}$ process, our numerical estimation show that

$$\delta\sigma_{\pm} = -0.38 \text{ pb} < 0 \quad (4.22)$$

for $m_{\pm} = 600 \text{ GeV}$ and $\beta = 0.76$. That means that the interference effect significantly decreases the H^{\pm} production cross section in this parameter region, thus the latter is not constrained by current LHC experiments.

4.3 Summary on Collider Constraints

The 125 GeV Higgs (H_1) signal strength measurements lead to a constraint $|\alpha_2| \lesssim 0.33$, which depends weakly on β . The LHC direct searches for heavy neutral scalars decaying to the ZZ final state set a stricter constraint $|\alpha_2| \lesssim 0.27$ for $m_2 = 500 \text{ GeV}$ in both Scenario (a) and (b). When $m_2 \gtrsim (550 - 600) \text{ GeV}$, the constraint from direct searches becomes weaker than that from the global fit on the H_1 signal strengths. In further analysis, we prefer to choose $\alpha_2 = 0.27$, which is the largest allowed value for $m_2 = 500 \text{ GeV}$. We have also checked the constraints from $t\bar{t}$, $t\bar{t}t\bar{t}$ and charged Higgs boson searches, in which the interference effects are very important. All benchmark points that we have considered are allowed by current LHC measurements. In the remainder of this work, we focus on the phenomenology of CP-violation in $t\bar{t}H_1$ associate production. We will instead consider the production and decay phenomenology of the heavy (pseudo)scalars $H_{2,3}$ in a forthcoming paper.

5 LHC Phenomenology of CP-violation in $t\bar{t}H_1$ Production

In this section, we study the production of the neutral Higgs bosons H_1 in association with a $t\bar{t}$ pair at the LHC. We start by discussing the setup used in the calculation and finish by highlighting the results for the $t\bar{t}H_1$ final state.

5.1 Phenomenological Setup

Events are generated at Leading Order (LO) using MADGRAPH5_AMC@NLO [118, 119]. Cross sections of signal processes are calculated using a UFO model file [123] corresponding to the general 2HDM [124] slightly modified to account for CP-violation effects in vertices involving both the neutral (H_i , with $i = 1, 2, 3$) and charged (H^{\pm}) Higgs boson states. Here, we employ the LO version of the MMHTLO68CL PDF sets [125]. For both the signal and background processes, we have used the nominal value for the (identical) renormalization and factorization scales to be equal to half the scalar sum of the transverse mass of all final state particles on an event-by-event basis, i.e.:

$$\mu_R = \mu_F = \frac{1}{2} \sum_{i=1}^N \sqrt{m_i^2 + p_{T,i}^2}. \quad (5.1)$$

In the computation of the parton level cross sections, we have employed the G_μ scheme, where the input parameters are G_F , α_{em} and m_Z , the numerical values of which are given by

$$\begin{aligned} G_F &= 1.16639 \times 10^{-5} \text{ GeV}^{-2}, \\ \alpha_{\text{em}}^{-1}(0) &= 137 \text{ and } m_Z = 91.188 \text{ GeV}. \end{aligned} \quad (5.2)$$

The values for m_W and $s_{\theta_W}^2$ are computed from the above inputs. For the pole masses of the fermions, we have taken

$$m_t = 172.5 \text{ GeV}, \quad m_b = 4.7 \text{ GeV}. \quad (5.3)$$

Uncertainties due to the scale and PDF variations are computed using SYSCALC [126]. In order to keep full spin correlations at both the production and decay stages of the top quarks, we have employed MADSPIN [127]. PYTHIA8 [128] is used to perform parton showering and hadronization – albeit without including Multiple Parton Interactions (MPIs) – to the events, eventually producing a set of event files in HEPMC format [129]. The HEPMC files are passed to RIVET (version 2.7.1) [130] for a particle level analysis. In the latter, jets are clustered using the anti- k_T algorithm using FASTJETS [131, 132]¹⁰.

The particle level events are selected if they contain charged leptons, high jet multiplicity of 4-6 jets where some of these are b -tagged (see below) and missing transverse energy which corresponds to the SM neutrino from W boson decays. Only prompt electrons and muons directly connected to the W boson are accepted, i.e., we do not select those coming from τ decays. Electrons are selected if they pass the basic selection requirement of $p_T^e > 30$ GeV and $|\eta^e| < 2.5$ while muons are selected if they satisfy the conditions $p_T^\mu > 27$ GeV and $|\eta^\mu| < 2.4$. Jets are clustered with jet radius $\Delta R = 0.4$ and selected if they satisfy $p_T^j > 30$ GeV and $|\eta^j| < 2.4$. For b -tagging, we use the so-called ghost-association technique [139, 140]. In this method, a jet is b -tagged if all the jet particles i within $\Delta R(\text{jet}, i) < 0.3$ of a given anti- k_T jet satisfy $p_T^i > 5$ GeV. Furthermore, in our analysis, we select events if they contain two charged leptons (with opposite electric charge), at least four jets (where at least two of them are b -tagged) and missing energy (coming from neutrinos in the leptonic decays of both top (anti)quarks).

5.2 Inclusive $t\bar{t}H_1$ Cross Section

The LO parton level Feynman diagrams are depicted in Figure 11. The cross section has two contributions: one from $q\bar{q}$ annihilation (diagram (a) in Figure 11), which is expected to dominate in the region of medium and large $x = \tilde{p}_i/P$ (with P being the longitudinal momentum of the incoming proton) and one from gg fusion (diagrams (b) and (c) in Figure 11) dominating at low x . For the calculation of the cross section, we employ MADGRAPH5_AMC@NLO [118, 119] with the MMHTLO68CL and MMHTNLO68CL PDF sets [125] in the 4-flavor scheme. Systematic uncertainties are divided into two categories: scale and

¹⁰Results were found to be stable if replacing PYTHIA8 with HERWIG6.5 [133–136] and the anti- k_T algorithm with the Cambridge-Aachen one [137, 138].

Figure 11. Representative Feynman diagrams corresponding to $t\bar{t}H_1$ production at LO. They consist of production through $q\bar{q}$ annihilation (diagram (a)) and through gg fusion (diagrams (b)-(c)).

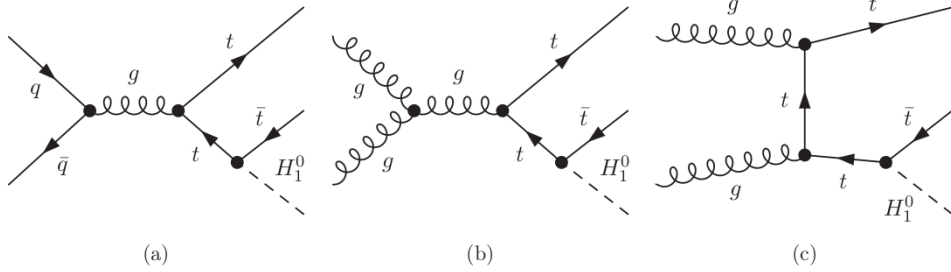


Table 8. Parton level cross sections for the production of $t\bar{t}H_1$ final states at the LHC at LO and NLO. The results are shown along with the theoretical uncertainties due to scale variations (first errors) and PDF uncertainties (second errors). The cross sections were computed for the cases of no cuts on the Higgs boson p_T (first row), for $p_T^H > 50$ GeV (second row) and for $p_T^H > 200$ GeV (third row).

	σ_{LO} [fb]	σ_{NLO} [fb]
No cuts	$398.9^{+32.7\%}_{-22.9\%}$ (scale) $^{+1.91\%}_{-1.54\%}$ (PDF)	$470.6^{+5.8\%}_{-9.0\%}$ (scale) $^{+2.2\%}_{-2.1\%}$ (PDF)
$p_T^H > 50$ GeV	$325.2^{+32.8\%}_{-22.9\%}$ (scale) $^{+1.96\%}_{-1.56\%}$ (PDF)	$382.8^{+5.4\%}_{-8.8\%}$ (scale) $^{+2.3\%}_{-2.1\%}$ (PDF)
$p_T^H > 200$ GeV	$55.6^{+33.9\%}_{-23.5\%}$ (scale) $^{+2.44\%}_{-1.81\%}$ (PDF)	$69.8^{+8.3\%}_{-10.6\%}$ (scale) $^{+2.9\%}_{-2.6\%}$ (PDF)

PDF ones. The scale uncertainties are obtained by varying the renormalization and factorization scales by a factor of two around their nominal value, i.e.,

$$(\mu_R, \mu_F) = \{(1, 1), (1, 0.5), (1, 2), (0.5, 1), (0.5, 0.5), (0.5, 2), (2, 1), (2, 0.5), (2, 2)\}(\mu_R^0, \mu_F^0), \quad (5.4)$$

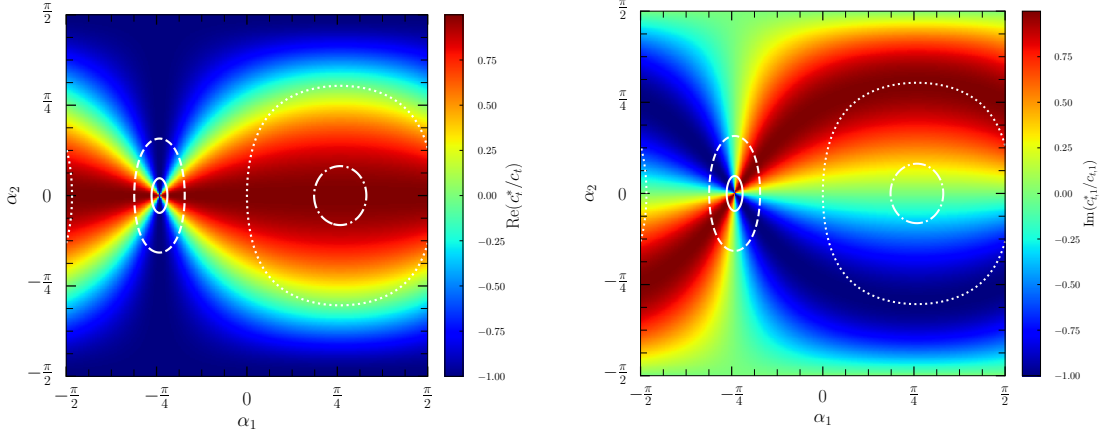
with

$$\mu_F^0 = \mu_R^0 = \frac{1}{2} \sum_i \sqrt{p_{T,i}^2 + m_i^2}. \quad (5.5)$$

Furthermore, PDF uncertainties are estimated using the HESSIAN method [141].

In Table 8, we show the results of the cross section both at LO and the Next-to-LO (NLO) in the SM. We can see that the NLO corrections imply a K -factor of about 1.17 in the case when no cuts are applied on the Higgs boson transverse momentum and for the case where $p_T^H > 50$ GeV. The K -factor slightly increase to 1.25 when a more stringent cut ($p_T^H > 200$ GeV) is applied. Furthermore, the theoretical uncertainties are dominated by those associated to scale variations which significantly decrease when we go from LO to NLO. PDF uncertainties are subleading and mildly dependent on the Higgs p_T cut.

Figure 12. The Real (left) and imaginary (right) parts of the ratio $c_{t,1}^*/c_{t,1}$ projected on the mixing angles α_1 and α_2 upon fixing $\beta = 0.76$. The solid, dashed, dotted and dot-dashed lines show the contours where $\sigma_{2\text{HDM}}(pp \rightarrow t\bar{t}H_1)/\sigma_{\text{SM}}(pp \rightarrow t\bar{t}H_1)$ is 0.01, 0.1, 1 and 2, respectively.



Finally, we notice that the ggF contribution is dominant accounting for $\simeq 68$ ($\simeq 71.5\%$), at LO(NLO), of the total cross section in the case of $p_T^H > 50$ GeV and slightly decreasing to $\simeq 59\%$ ($\simeq 67\%$) for the $p_T^H > 200$ GeV case.

In the 2HDM, the $t\bar{t}H_1$ coupling is given by

$$\mathcal{L}_{t\bar{t}H_1} = -\frac{m_t}{v} (c_{t,1}\bar{t}_L t_R H_1 + \text{H.c.}), \quad (5.6)$$

with $c_{t,1} = c_{\alpha_2} s_{\beta+\alpha_1}/s_\beta - i s_{\alpha_2}/t_\beta$ (see Equation A.1) for all four types of models. The $t\bar{t}H_1$ production cross section behaves as shown in Equation 4.4. The presence of the pseudoscalar part in the $t\bar{t}H_1$ coupling can drastically changes the value of the cross section as can be seen in Figure 12.

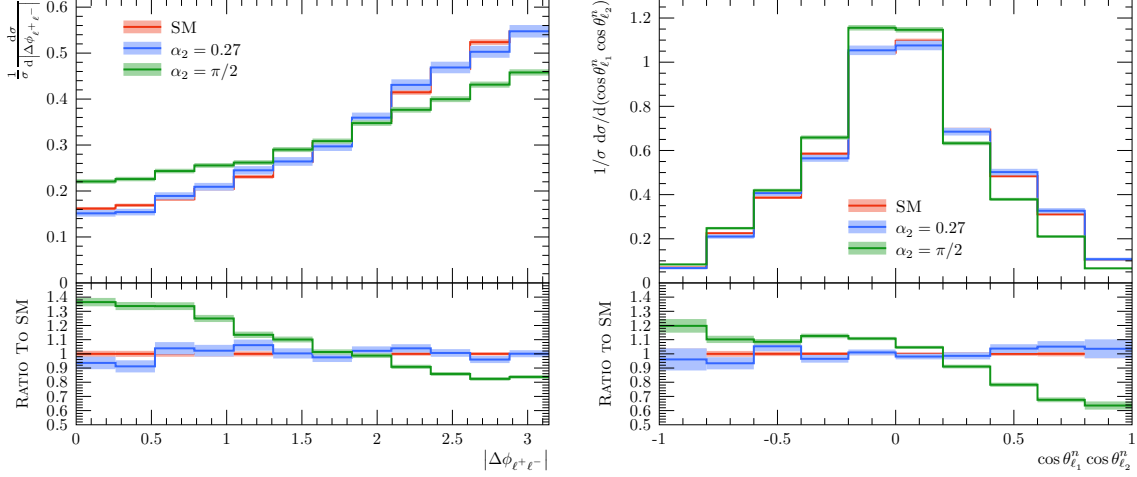
5.3 Results

In this subsection, we show the results of the sensitivity of certain spin observables to the nature of the $t\bar{t}H_1$ vertex. Description of the observables is given in Appendix F. In Figure 13, we show the results of the normalized distributions corresponding to spin observables in the SM (red lines) and the 2HDM with $\alpha_2 = 0.27$ (blue lines). The pure pseudoscalar case $\alpha_2 = \pi/2$ is also shown in green lines as a comparison in the figures. To avoid clutter, we show only the most sensitive observables, i.e., the difference in the azimuthal angles of the charged leptons and the $\cos\theta_{\ell^+}^n \cos\theta_{\ell^-}^n$ spectrum in the transverse basis.

In order to quantify the sensitivity of the various spin observables to the benchmark points, we compute forward-backward asymmetries. An asymmetry $\mathcal{A}_{\mathcal{O}}$ on the observable \mathcal{O} is defined by

$$\mathcal{A}_{\mathcal{O}} = \frac{N(\mathcal{O} > \mathcal{O}_c) - N(\mathcal{O} < \mathcal{O}_c)}{N(\mathcal{O} > \mathcal{O}_c) + N(\mathcal{O} < \mathcal{O}_c)}, \quad (5.7)$$

Figure 13. *Left:* Normalized differential cross section $1/\sigma d\sigma/d|\Delta\phi_{\ell^+\ell^-}|$ versus $|\Delta\phi_{\ell^+\ell^-}|$ in the laboratory frame. *Right:* Normalized differential distribution $(1/\sigma)d\sigma/d(\cos\theta_{\ell_a}^n \cos\theta_{\ell_b}^n)$ versus $\cos\theta_{\ell_a} \cos\theta_{\ell_b}$ in the transverse basis. The distributions are shown for the SM (red) and for the selected benchmark point, $\alpha_2 = 0.27$, of the Type III 2HDM (blue). We also show the distribution for the pure pseudoscalar case $\alpha_2 = \pi/2$ in green lines as a comparison, which is of course excluded.



where \mathcal{O}_c is a reference point for the observable \mathcal{O} with respect to which the asymmetry is evaluated. For angular (energy) observables, we choose $\mathcal{O}_c = 0$ ($\mathcal{O}_c = 0.5$).

To quantify deviations from the SM expectations, we compute the χ^2 as

$$\chi^2 = \frac{(\mathcal{A}_{\mathcal{O}} - \mathcal{A}_{\mathcal{O}}^{\text{SM}})^2}{\sigma_{\mathcal{O}}^2}, \quad (5.8)$$

with $\sigma_{\mathcal{O}}$ the uncertainty on the measurement of the asymmetry in the SM. We assume that the asymmetry follows a Gaussian distribution, in which case the uncertainty is given by [142]

$$\sigma_{\mathcal{O}} = \sqrt{\frac{1 - \mathcal{A}_{\mathcal{O}}^2}{N}}, \quad (5.9)$$

where $N = A \times \epsilon \times \mathcal{L}$. Here, $A \times \epsilon$ is the acceptance times the efficiency of the signal process after full selection. In our case, we find that the efficiency is about 14% for both the SM and the 2HDM, at $\mathcal{L} = 3000 \text{ fb}^{-1}$, and σ is the cross section times the BRs, i.e.,

$$\sigma = \sigma(t\bar{t}H_1) \times \text{BR}(H_1 \rightarrow b\bar{b}) \times \text{BR}(t \rightarrow b\nu)^2. \quad (5.10)$$

In this calculation, we assume a b -tagging efficiency of about 80%. In Table 9, we show the expected deviations from the SM expectation at $\mathcal{L} = 3000 \text{ fb}^{-1}$. We can see that, unfortunately, for $\alpha_2 = 0.27$, the χ^2 cannot be larger than 0.93 considering only a single observable. After combining all the observables in Table 9, the χ^2 can reach about 4.4. The results depends weakly on β and α_1 in our favored region ($t_\beta \sim 1$ and $\alpha_1 \sim 0$), because the observables are sensitive only to the $t\bar{t}H_1$ CP-violating phase $\simeq s_{\alpha_2}/t_\beta$ in this

Table 9. Values of the asymmetries for the SM and 2HDM with $\alpha_2 = 0.27$. The values of the χ^2 quantifying the deviations from the SM expectations are shown in the fourth column. The computations are performed for an integrated luminosity of 3000 fb^{-1} . The shorthand notations $c_{\ell+}^r = \cos \theta_{\ell+}^k, \dots$ are used. Details about the calculations are discussed in the text.

Asymmetry	SM	($\alpha_2 = 0.27$)	χ_{BF}^2
$\cos \theta_{\ell}^k$	5.02×10^{-3}	3.98×10^{-3}	1.91×10^{-3}
$\cos \theta_{\ell}^n$	3.13×10^{-3}	3.27×10^{-3}	3.51×10^{-5}
$\cos \theta_{\ell}^r$	4.30×10^{-3}	-1.05×10^{-2}	0.39
$\cos \varphi_{\ell+\ell-}$	3.52×10^{-2}	5.58×10^{-2}	0.75
$\cos \theta_{\ell H}$	-0.12	-0.11	8.62×10^{-2}
u	-0.21	-0.22(2)	0.15
x_{ℓ}	0.82(5)	0.82(2)	7.08×10^{-2}
z	-0.40	-0.41	0.18
$\cos \theta_{\ell+}^k \cos \theta_{\ell-}^k$	5.58×10^{-3}	1.01×10^{-2}	3.74×10^{-2}
$\cos \theta_{\ell+}^n \cos \theta_{\ell-}^n$	7.40×10^{-2}	7.90×10^{-2}	4.44×10^{-2}
$\cos \theta_{\ell+}^r \cos \theta_{\ell-}^r$	2.74×10^{-2}	2.85×10^{-2}	2.14×10^{-3}
$c_{\ell+}^k c_{\ell-}^n + c_{\ell-}^k c_{\ell+}^n$	-7.58×10^{-3}	1.26×10^{-2}	0.73
$c_{\ell+}^k c_{\ell-}^n - c_{\ell-}^k c_{\ell+}^n$	-2.79×10^{-3}	-1.90×10^{-2}	0.47
$c_{\ell+}^k c_{\ell-}^r + c_{\ell-}^k c_{\ell+}^r$	3.09×10^{-3}	-8.93×10^{-3}	0.26
$c_{\ell+}^k c_{\ell-}^r - c_{\ell-}^k c_{\ell+}^r$	-3.23×10^{-2}	-3.56×10^{-2}	1.90×10^{-2}
$c_{\ell+}^r c_{\ell-}^n + c_{\ell-}^r c_{\ell+}^n$	1.39×10^{-3}	-1.21×10^{-2}	0.32
$c_{\ell+}^r c_{\ell-}^n - c_{\ell-}^r c_{\ell+}^n$	4.00×10^{-3}	3.27×10^{-3}	9.41×10^{-4}
$\Delta \phi_{\ell+\ell-}$	0.38	0.36	0.93

region. Possible improvements may be made by using, e.g., the $\cos \theta_{\ell}$ in the r -basis (see [Appendix F](#)) in the “single lepton plus jets” final state.

6 Conclusions

In this work, we have analyzed soft CP-violating effects in both EDMs and LHC phenomenology in a 2HDM with soft CP-violation. In this scenario, the mixing angle α_2 is the key parameter measuring the size of CP-violation since the CP-violating phases in $H_1 f \bar{f}$ Yukawa vertices are proportional to s_{α_2} .

We have considered all four standard types of Yukawa couplings, named Type I-IV models, in our analysis. In Type I and IV models, there is no cancellation mechanism in electron EDM calculations, leading to a very strict constraint on the CP-violating phase $|\arg c_{t/\tau,1}| \lesssim 8.5 \times 10^{-4}$, which renders all CP-violating effects unobservable in further collider studies for these two models.

In Type II and III models, we have discussed two scenarios: (a) $H_{2,3}$ are closed in mass while α_3 is away from 0 or $\pi/2$; and (b) $H_{2,3}$ have a large mass splitting while α_3 must appear close to 0 or $\pi/2$. The cancellation behavior in the electron EDM leads to a larger allowed region for α_2 in both scenarios. In such two models, t_{β} is favored to be close to 1, whose location depends on the masses of the heavy (pseudo)scalars, with a strong correlation with α_1 . The electron EDM alone cannot set constraints on α_2 directly. In the

Type II model, $|\alpha_2| \lesssim 0.09$ is estimated from the neutron EDM constraint if we consider only the central value estimation and this constraint can be as weak as $\lesssim 0.15$ if theoretical uncertainty in neutron EDM estimation is also considered. In the Type III model, no constraint can be drawn from the neutron EDM and $|\alpha_2| \lesssim 0.27$ is estimated from LHC constraints if $m_2 \simeq 500$ GeV. Other LHC direct searches do not set further limits for the 2HDM.

Our analysis shows the importance of further neutron EDM measurements to an accuracy of $\mathcal{O}(10^{-27} e \cdot \text{cm})$. An α_2 of the size $\sim \mathcal{O}(0.1)$ will lead to significantly non-zero results in such experiments. If CP-violation in the Higgs sector exists, as we have discussed, first evidence of it is expected to appear in the neutron EDM measurements. Conversely, if there is still a null result for the neutron EDM, constraints on $|\alpha_2|$ can be pushed to about 4×10^{-3} in the Type II model and 2×10^{-2} in the Type III model. Thus, we conclude that, for models in which a cancellation mechanism can appear in the electron EDM, the neutron EDM measurements are good supplements to find evidence of CP-violation or set constraints on the CP-violating angle directly.

We have also performed a phenomenological study of soft CP-violation in the 2HDM for the case of $t\bar{t}H_1$ associate production at the LHC with a luminosity of 3000 fb^{-1} . With fixed β and $\alpha_{1,2}$, its properties are independent of the mixing angle α_3 and the masses of the heavy (pseudo)scalars $H_{2,3}$ and H^\pm . Upon choosing the benchmark point $\beta = 0.76$, $\alpha_1 = 0.02$ and $\alpha_2 = 0.27$, we constructed top (anti)quark spin dependent observables and tested their deviations from the SM. Amongst these, a single observable, the azimuthal angle between the two leptons from fully leptonic $t\bar{t}$ decays, $\Delta\phi_{\ell+\ell^-}$, is the most sensitive one, with $\chi^2 = 0.93$, meaning that we can hardly achieve any higher signal significance using any other single observable. After combining all the observables, χ^2 can reach 4.4. In the light of this, then, we conclude that future neutron EDM experiments could provide more useful tests of soft CP-violation in the 2HDM than the LHC experiments.

In this paper, we did not perform phenomenological studies of the heavy (pseudo)scalars ($H_{2,3}$ or H^\pm), for which interference effects with the SM background are very important and thus need a dedicated treatment. We will turn to them in a forthcoming paper.

Acknowledgements

We thank Abdesslam Arhrib, Jianqi Chen, Qi-Shu Yan, Hao Zhang, and Shou-hua Zhu for helpful discussion. We also thank Abdesslam Arhrib for collaboration at the beginning of this project. This work was supported in part by the MoST of Taiwan under the grant no. 107-2112-M-007-029-MY3. The work of AJ was supported by the National Research Foundation of Korea under grant no. NRF-2019R1A2C1009419. AJ would like to thank the CERN Theory Department for hospitality where part of this work has been done. SM is supported in part through the NExT Institute and the STFC CG ST/L000296/1 award.

A Yukawa Couplings

Following the parameterization in [Equation 2.15](#), we list the Yukawa couplings in the mass eigenstate basis explicitly [\[47–49\]](#) in terms of the mixing angles $\beta, \alpha_{1,2,3}$. By denoting with

$c_{f,i}^X$ the Yukawa coupling $c_{f,i}$ in the 2HDM Type X ($X = \text{I} - \text{IV}$) below, we have the following:

$$c_{U_i,1}^{\text{I-IV}} = \frac{c_{\alpha_2} s_{\beta+\alpha_1}}{s_{\beta}} - i \frac{s_{\alpha_2}}{t_{\beta}}, \quad (\text{A.1})$$

$$c_{U_i,2}^{\text{I-IV}} = \frac{c_{\beta+\alpha_1} c_{\alpha_3} - s_{\beta+\alpha_1} s_{\alpha_2} s_{\alpha_3}}{s_{\beta}} - i \frac{c_{\alpha_2} s_{\alpha_3}}{t_{\beta}}, \quad (\text{A.2})$$

$$c_{U_i,3}^{\text{I-IV}} = -\frac{c_{\beta+\alpha_1} s_{\alpha_3} + s_{\beta+\alpha_1} s_{\alpha_2} c_{\alpha_3}}{s_{\beta}} - i \frac{c_{\alpha_2} c_{\alpha_3}}{t_{\beta}}, \quad (\text{A.3})$$

$$c_{D_i,1}^{\text{I,III}} = \frac{c_{\alpha_2} s_{\beta+\alpha_1}}{s_{\beta}} + i \frac{s_{\alpha_2}}{t_{\beta}},$$

$$c_{D_i,1}^{\text{II,IV}} = \frac{c_{\alpha_2} c_{\beta+\alpha_1}}{c_{\beta}} - i s_{\alpha_2} t_{\beta}, \quad (\text{A.4})$$

$$c_{D_i,2}^{\text{I,III}} = \frac{c_{\beta+\alpha_1} c_{\alpha_3} - s_{\beta+\alpha_1} s_{\alpha_2} s_{\alpha_3}}{s_{\beta}} + i \frac{c_{\alpha_2} s_{\alpha_3}}{t_{\beta}},$$

$$c_{D_i,2}^{\text{II,IV}} = -\frac{s_{\beta+\alpha_1} c_{\alpha_3} + c_{\beta+\alpha_1} s_{\alpha_2} s_{\alpha_3}}{c_{\beta}} - i c_{\alpha_2} s_{\alpha_3} t_{\beta}, \quad (\text{A.5})$$

$$c_{D_i,3}^{\text{I,III}} = -\frac{c_{\beta+\alpha_1} s_{\alpha_3} + s_{\beta+\alpha_1} s_{\alpha_2} c_{\alpha_3}}{s_{\beta}} + i \frac{c_{\alpha_2} c_{\alpha_3}}{t_{\beta}},$$

$$c_{D_i,3}^{\text{II,IV}} = \frac{s_{\beta+\alpha_1} s_{\alpha_3} - c_{\beta+\alpha_1} s_{\alpha_2} c_{\alpha_3}}{c_{\beta}} - i c_{\alpha_2} c_{\alpha_3} t_{\beta}, \quad (\text{A.6})$$

$$c_{\ell_i,1}^{\text{I,IV}} = \frac{c_{\alpha_2} s_{\beta+\alpha_1}}{s_{\beta}} + i \frac{s_{\alpha_2}}{t_{\beta}},$$

$$c_{\ell_i,1}^{\text{II,III}} = \frac{c_{\alpha_2} c_{\beta+\alpha_1}}{c_{\beta}} - i s_{\alpha_2} t_{\beta}, \quad (\text{A.7})$$

$$c_{\ell_i,2}^{\text{I,IV}} = \frac{c_{\beta+\alpha_1} c_{\alpha_3} - s_{\beta+\alpha_1} s_{\alpha_2} s_{\alpha_3}}{s_{\beta}} + i \frac{c_{\alpha_2} s_{\alpha_3}}{t_{\beta}},$$

$$c_{\ell_i,2}^{\text{II,III}} = -\frac{s_{\beta+\alpha_1} c_{\alpha_3} + c_{\beta+\alpha_1} s_{\alpha_2} s_{\alpha_3}}{c_{\beta}} - i c_{\alpha_2} s_{\alpha_3} t_{\beta}, \quad (\text{A.8})$$

$$c_{\ell_i,3}^{\text{I,IV}} = -\frac{c_{\beta+\alpha_1} s_{\alpha_3} + s_{\beta+\alpha_1} s_{\alpha_2} c_{\alpha_3}}{s_{\beta}} + i \frac{c_{\alpha_2} c_{\alpha_3}}{t_{\beta}},$$

$$c_{\ell_i,3}^{\text{II,III}} = \frac{s_{\beta+\alpha_1} s_{\alpha_3} - c_{\beta+\alpha_1} s_{\alpha_2} c_{\alpha_3}}{c_{\beta}} - i c_{\alpha_2} c_{\alpha_3} t_{\beta}. \quad (\text{A.9})$$

B Scalar Couplings

The scalar couplings in the potential can be expressed using the physical parameters as [47–49]

$$\lambda_1 = \frac{1}{c_\beta^2 v^2} \left[c_{\beta+\alpha_1}^2 c_{\alpha_2}^2 m_1^2 + (c_{\beta+\alpha_1} s_{\alpha_2} s_{\alpha_3} + s_{\beta+\alpha_1} c_{\alpha_3})^2 m_2^2 + (c_{\beta+\alpha_1} s_{\alpha_2} c_{\alpha_3} - s_{\beta+\alpha_1} s_{\alpha_3})^2 m_3^2 - s_\beta^2 \mu^2 \right], \quad (\text{B.1})$$

$$\lambda_2 = \frac{1}{s_\beta^2 v^2} \left[s_{\beta+\alpha_1}^2 c_{\alpha_2}^2 m_1^2 + (c_{\beta+\alpha_1} c_{\alpha_3} - s_{\beta+\alpha_1} s_{\alpha_2} s_{\alpha_3})^2 m_2^2 + (s_{\beta+\alpha_1} s_{\alpha_2} c_{\alpha_3} + c_{\beta+\alpha_1} s_{\alpha_3})^2 m_3^2 - c_\beta^2 \mu^2 \right], \quad (\text{B.2})$$

$$\lambda_3 = \frac{1}{s_{2\beta} v^2} \left[s_{2(\beta+\alpha_1)} (c_{\alpha_2}^2 m_1^2 + (s_{\alpha_2}^2 s_{\alpha_3}^2 - c_{\alpha_3}^2) m_2^2 + (s_{\alpha_2}^2 c_{\alpha_3}^2 - s_{\alpha_3}^2) m_3^2) + s_{\alpha_2} s_{2\alpha_3} c_{2(\beta+\alpha_1)} (m_3^2 - m_2^2) \right] + \frac{2m_\pm^2 - \mu^2}{v^2}, \quad (\text{B.3})$$

$$\lambda_4 = \frac{1}{v^2} (s_{\alpha_2}^2 m_1^2 + c_{\alpha_2}^2 s_{\alpha_3}^2 m_2^2 + c_{\alpha_2}^2 c_{\alpha_3}^2 m_3^2 + \mu^2 - 2m_\pm^2), \quad (\text{B.4})$$

$$\lambda_5 = \frac{1}{v^2} (\mu^2 - s_{\alpha_2}^2 m_1^2 - c_{\alpha_2}^2 s_{\alpha_3}^2 m_2^2 - c_{\alpha_2}^2 c_{\alpha_3}^2 m_3^2) - \frac{i}{s_{2\beta} v^2} \left[c_\beta (c_{\beta+\alpha_1} s_{2\alpha_2} m_1^2 - (c_{\beta+\alpha_1} s_{2\alpha_2} s_{\alpha_3}^2 + s_{\beta+\alpha_1} c_{\alpha_2} s_{2\alpha_3}) m_2^2 + (s_{\beta+\alpha_1} c_{\alpha_2} s_{2\alpha_3} - c_{\beta+\alpha_1} s_{2\alpha_2} c_{\alpha_3}^2) m_3^2) + s_\beta (s_{\beta+\alpha_1} s_{2\alpha_2} m_1^2 + (c_{\beta+\alpha_1} c_{\alpha_2} s_{2\alpha_3} - s_{\beta+\alpha_1} s_{2\alpha_2} s_{\alpha_3}^2) m_2^2 - (c_{\beta+\alpha_1} c_{\alpha_2} s_{2\alpha_3} + s_{\beta+\alpha_1} s_{2\alpha_2} c_{\alpha_3}^2) m_3^2) \right]. \quad (\text{B.5})$$

Consider the-bounded-from-below conditions as [45]

$$\lambda_1 > 0, \quad \lambda_2 > 0, \quad \lambda_3 > -\sqrt{\lambda_1 \lambda_2}, \quad \lambda_3 + \lambda_4 - |\lambda_5| > -\sqrt{\lambda_1 \lambda_2}, \quad (\text{B.6})$$

then $\mu^2 \lesssim (450 \text{ GeV})^2$ is favored and thus we choose $\mu^2 = (450 \text{ GeV})^2$ in the analysis.

The couplings between neutron and charged scalars $c_{i,\pm}$ are [49]

$$c_{i,\pm} = c_\beta (s_\beta^2 (\lambda_1 - \lambda_4 - \text{Re}(\lambda_5)) + c_\beta^2 \lambda_3) R_{i1} + s_\beta (c_\beta^2 (\lambda_2 - \lambda_4 - \text{Re}(\lambda_5)) + s_\beta^2 \lambda_3) R_{i2} + s_\beta c_\beta \text{Im}(\lambda_5) R_{i3}, \quad (\text{B.7})$$

where R is the matrix in Equation 2.8. These couplings are useful in the calculations of fermionic EDMs seeing the contribution of a charged Higgs boson.

C Loop Integrations for EDM

The loop functions in the calculation of the Barr-Zee diagrams are [68–74]:

$$f(z) = \frac{z}{2} \int_0^1 dx \frac{1-2x(1-x)}{x(1-x)-z} \ln \left(\frac{x(1-x)}{z} \right), \quad (\text{C.1})$$

$$g(z) = \frac{z}{2} \int_0^1 dx \frac{1}{x(1-x)-z} \ln \left(\frac{x(1-x)}{z} \right), \quad (\text{C.2})$$

$$h(z) = \frac{z}{2} \int_0^1 dx \frac{1}{x(1-x)-z} \left[\frac{z}{x(1-x)-z} \ln \left(\frac{x(1-x)}{z} \right) - 1 \right], \quad (\text{C.3})$$

$$F(x, y) = \frac{yf(x) - xf(y)}{y-x}; \quad G(x, y) = \frac{yg(x) - xg(y)}{y-x}, \quad (\text{C.4})$$

$$H_i^a(z) = z \int_0^1 dx \frac{(1-x)^2(x-4+x(z_{\pm, W} - z_{WH_i}^{-1}))}{x+(1-x)z_{WH_i} - x(1-x)z} \ln \left(\frac{x+(1-x)z_{WH_i}}{x(1-x)z} \right), \quad (\text{C.5})$$

$$H_i^b(z) = 2z \int_0^1 dx \frac{x(1-x)^2}{x+(1-x)z_{\pm, i} - x(1-x)z} \ln \left(\frac{x+(1-x)z_{\pm, i}}{x(1-x)z} \right). \quad (\text{C.6})$$

Denoting

$$a_x = x(1-x), \quad b = a_x/z_a, \quad A = x+y/z_a, \quad B = A - a_x, \quad B' = A - a_y, \\ C = \frac{A}{B} \ln \frac{A}{a_x} - 1, \quad C' = \frac{a_x}{B} \ln \frac{A}{a_x} - 1, \quad C'' = \frac{a_y}{B'} \ln \frac{A}{a_y} - 1, \quad (\text{C.7})$$

the loop functions in the non-Barr-Zee type diagrams with a W boson are [70]

$$(D_W^a)_i = -\frac{1}{2} \int_0^1 dx \int_0^{1-x} dy \frac{x}{B} \left[\frac{2C}{B} (3A - 2xy) - 3 + \frac{2xy}{a_x} \right], \quad (\text{C.8})$$

$$(D_W^b)_i = \int_0^1 dx \int_0^{1-x} dy x \left[C' \left(\frac{3A - 2xy}{B^2} + \frac{1 + \frac{3x}{2a_x}(1-2y+B)}{B} \right) + \frac{3A - 2xy}{2a_x B} \right], \quad (\text{C.9})$$

$$(D_W^c)_i = \int_0^1 dx \int_0^{1-x} dy \frac{x^2 y}{a_x(1-y-b)} \left[\frac{b}{1-y-b} \ln \frac{1-y}{b} - 1 \right], \quad (\text{C.10})$$

$$(D_W^d)_i = -\frac{1}{8} \int_0^1 dx \int_0^{1-x} dy \left[\frac{1}{Bz_{WH_i}} \left(1 - \frac{2Ca_x}{B} \right) + \frac{x}{B} \left(1 - \frac{2CA}{B} \right) \right], \quad (\text{C.11})$$

$$(D_W^e)_i = \frac{1}{8} \int_0^1 dx \int_0^{1-x} dy \frac{x}{a_x} \\ \times \left[\frac{C'}{B^2} (xa_x(2x-1) + Bx(3x-1) - 2B^2) - 2 + \frac{x(2x-1)}{2B} \right]. \quad (\text{C.12})$$

The loop functions in the non-Barr-Zee type diagrams with a Z boson are instead [70]

$$(D_Z^a)_i = \int_0^1 dx \int_0^{1-x} dy \frac{2x}{a_x} \left[1 + C' \left(1 + \frac{x(1-x-y)}{2B} \right) \right], \quad (\text{C.13})$$

$$(D_Z^b)_i = \int_0^1 dx \int_0^{1-x} dy \frac{x^2 y}{a_x(1-y-b)} \left[\frac{b}{1-y-b} \ln \frac{1-y}{b} - 1 \right], \quad (\text{C.14})$$

$$(D_Z^c)_i = \int_0^1 dx \int_0^{1-x} dy \frac{1}{a_y} \left[y - x + C'' \left(y - x + \frac{y^2(1-x-y)}{B'} \right) \right]. \quad (\text{C.15})$$

In the functions $(D_W^p)_i$, we have $z_a \equiv z_{WH_i}$ while, in the functions $(D_Z^p)_i$, we have $z_a \equiv z_{ZH_i}$. Last, the loop function for the Weinberg operator is [72]

$$W(z) = 4z^2 \int_0^1 dv \int_0^1 du \frac{(1-v)(uv)^3}{[zv(1-uv) + (1-u)(1-v)]^2}. \quad (\text{C.16})$$

D Loop Integrations for Higgs Production and Decay

The loop functions for Higgs production and decay are [106, 107]

$$\mathcal{A}_0(x) = \frac{x - I(x)}{x^2}, \quad (\text{D.1})$$

$$\mathcal{A}_1(x) = -\frac{x + (x-1)I(x)}{x^2}, \quad (\text{D.2})$$

$$\mathcal{A}_2(x) = \frac{2x^2 + 3x + 3(2x-1)I(x)}{x^2}, \quad (\text{D.3})$$

$$\mathcal{B}_1(x) = -2\frac{I(x)}{x}, \quad (\text{D.4})$$

where

$$I(z) = \begin{cases} \arcsin^2(\sqrt{z}), & z \leq 1, \\ -\frac{1}{4} \left[\ln \left(\frac{1+\sqrt{1-z^{-1}}}{1-\sqrt{1-z^{-1}}} \right) - i\pi \right]^2, & z > 1. \end{cases} \quad (\text{D.5})$$

E Decay of Heavy (Pseudo)scalars

For heavy neutral (pseudo)scalars, we consider the decay channels $H_{2,3} \rightarrow t\bar{t}, WW, ZZ$ and ZH_1 . The partial decay widths are given by

$$\Gamma_{H_i \rightarrow t\bar{t}} = \frac{3m_i m_t^2}{8\pi v^2} \left[[\text{Re}(c_{t,i})]^2 \left(1 - \frac{4m_t^2}{m_i^2}\right)^{\frac{3}{2}} + [\text{Im}(c_{t,i})]^2 \left(1 - \frac{4m_t^2}{m_i^2}\right)^{\frac{1}{2}} \right], \quad (\text{E.1})$$

$$\Gamma_{H_i \rightarrow WW} = \frac{m_i^3 c_{V,i}^2}{16\pi v^2} \sqrt{1 - \frac{4m_W^2}{m_i^2}} \left(1 - \frac{4m_W^2}{m_i^2} + \frac{12m_W^4}{m_i^4}\right), \quad (\text{E.2})$$

$$\Gamma_{H_i \rightarrow ZZ} = \frac{m_i^3 c_{V,i}^2}{32\pi v^2} \sqrt{1 - \frac{4m_Z^2}{m_i^2}} \left(1 - \frac{4m_Z^2}{m_i^2} + \frac{12m_Z^4}{m_i^4}\right), \quad (\text{E.3})$$

$$\Gamma_{H_i \rightarrow ZH_1} = \frac{m_i^3 c_{V,k}^2}{32\pi v^2} \mathcal{F}_{VS} \left(\frac{m_Z^2}{m_i^2}, \frac{m_i^2}{m_i^2} \right). \quad (\text{E.4})$$

Here $k \neq i$ or 1, and the functions

$$\mathcal{F}_{VS}(x, y) = (1 + x^2 + y^2 - 2x - 2y - 2xy)^{\frac{3}{2}}. \quad (\text{E.5})$$

In Scenario (b), since $H_{2,3}$ have large mass splitting, we should also consider the $H_3 \rightarrow ZH_2$ decay. Its partial width is

$$\Gamma_{H_3 \rightarrow ZH_2} = \frac{m_3^3 c_{V,1}^2}{32\pi v^2} \mathcal{F}_{VS} \left(\frac{m_Z^2}{m_3^2}, \frac{m_2^2}{m_3^2} \right). \quad (\text{E.6})$$

Thus numerically the total decay widths $\Gamma_{2,3}$ can reach about 20 GeV if $m_{2,3} \simeq 500$ GeV, and they both dominantly decay to $t\bar{t}$. In Scenario (b), if $m_2 = 500$ GeV and $m_3 = 650$ GeV, $\text{Br}_{H_3 \rightarrow ZH_2}$ can reach about 10%.

The charged Higgs boson H^\pm decays mainly to $t\bar{b}$ in the small t_β region. Ignoring the coupling term proportional to m_b , we have

$$\Gamma_{H^\pm \rightarrow t\bar{b}} = \frac{3m_\pm}{8\pi v^2} \left(\frac{m_t}{t_\beta} \right)^2 \left(1 - \frac{m_t^2}{m_\pm^2} \right)^2. \quad (\text{E.7})$$

Besides this, H^\pm also have subdominant decay channels, like $W^\pm H_i$ [49], yielding

$$\Gamma_{H^\pm \rightarrow W^\pm H_i} = \frac{m_\pm^3 (1 - c_{V,i}^2)}{16\pi v^2} \mathcal{F}_{VS} \left(\frac{m_W^2}{m_\pm^2}, \frac{m_i^2}{m_\pm^2} \right). \quad (\text{E.8})$$

For $\beta = 0.76$ and $m_\pm = 600$ GeV, $\Gamma_{H^\pm \rightarrow t\bar{b}} = 33$ GeV while the sum for all three neutral scalars $\sum_i \Gamma_{H^\pm \rightarrow W^\pm H_i} \lesssim 5$ GeV for $|\alpha_2| \lesssim 0.27$.

F CP-violation Observables in the $t\bar{t}H_1$ Channel

In this section, we give an overview of the different observables that we have used in this study to pin-down the spin and CP properties of the SM-like Higgs boson produced in association with a $t\bar{t}$ pair.

First, one can study directly the spin-spin correlations of the $t\bar{t}$ pair by measuring the differential distribution in $\cos\theta_{\ell^a}\cos\theta_{\ell^b}$ of the emerging leptons,

$$\frac{1}{\sigma} \frac{d^2\sigma}{d\cos\theta_{\ell^a}d\cos\theta_{\ell^b}} = \frac{1}{4} \left(1 + \alpha_{\ell^a} P_a \cos\theta_{\ell^a} + \alpha_{\ell^b} P_b \cos\theta_{\ell^b} + \alpha_{\ell^a} \alpha_{\ell^b} C_{ab} \cos\theta_{\ell^a} \cos\theta_{\ell^b} \right), \quad (\text{F.1})$$

where α_ℓ is the spin analyzing power of the charged lepton and $\theta_{\ell^{a,b}} = \angle(\hat{\ell}^{a,b}, \hat{S}_{a,b})$, with $\hat{\ell}^{a,b}$ being the direction of flight of the charged lepton in the top quark rest frame and $\hat{S}_{a,b}$ the spin quantization axis in the basis a . Furthermore, C_{ab} is the correlation coefficient which is related to the expectation value of $\cos\theta_{\ell^a}\cos\theta_{\ell^b}$ using Equation F.1. In the following, we consider three different bases: the helicity basis ($a = k$), the transverse basis ($a = n$) and the r -basis, see, e.g., [20, 143] for more details about the definitions of the spin bases and [144, 145] for reported measurements of these observables in $t\bar{t}$ production. It was found that the $t\bar{t}$ spin-spin correlations in the transverse and r -bases are good probes of CP-violation, e.g., through the anomalous chromomagnetic and chromoelectric top quark couplings [143]¹¹.

Furthermore, we consider the opening angle between the two oppositely charged leptons produced in the decays of the top (anti)quarks which is defined by

$$\cos\varphi_{\ell^a\ell^b} = \frac{\hat{p}_{\ell^+} \cdot \hat{p}_{\ell^-}}{|\hat{p}_{\ell^+}| |\hat{p}_{\ell^-}|}, \quad (\text{F.2})$$

where $\hat{p}_{\ell^+}(\hat{p}_{\ell^-})$ is the direction of the flight of the charged lepton $\ell^+(\ell^-)$ in the parent top (anti)quark rest frame.

The azimuthal angle $\Delta\phi_{\ell^+\ell^-} = |\phi_{\ell^+} - \phi_{\ell^-}|$ is a clean observable to measure the spin-spin correlations between the top and the antitop quarks. The momenta of the charged leptons are usually measured in the laboratory frame [146, 147]. This observable shows a high sensitivity to the degree of correlations between the top (anti)quarks in $t\bar{t}$ production. However, since we are considering the $t\bar{t}H_1$ production mode, the presence of the Higgs boson may wash out the sensitivity of $\Delta\phi$ to the correlations, though we have found this not to be the case.

In addition to the aforementioned observables, we also study the sensitivity of the following angle [21]

$$\cos\theta_{\ell H_1} = \frac{(\hat{p}_{\ell^+} \times \hat{p}_{H_1}) \cdot (\hat{p}_{\ell^-} \times \hat{p}_{H_1})}{|(\hat{p}_{\ell^+} \times \hat{p}_{H_1})| |(\hat{p}_{\ell^-} \times \hat{p}_{H_1})|}, \quad (\text{F.3})$$

¹¹In $t\bar{t}H_1$ production, the contribution of ggF is about 70% of the total cross section. Hence, the initial state is mostly Bose-symmetric. Following the recommendations of [143], the value of $\cos\theta_\ell$ is multiplied by the sign of the scattering angle $\vartheta = \hat{\mathbf{p}} \cdot \hat{\mathbf{p}}_t$ with $\hat{\mathbf{p}}_t = \mathbf{p}_t/|\mathbf{p}_t|$ the top quark direction of flight in the $t\bar{t}$ rest frame and $\hat{\mathbf{p}} = (0, 0, 1)$.

where \hat{p}_{ℓ^+} , \hat{p}_{ℓ^-} and \hat{p}_{H_1} are the directions of flight of the positively-, negatively charged lepton and of the reconstructed Higgs boson in the laboratory frame. The $\theta_{\ell H_1}$ angle defines the angle spanned by the charged lepton momenta projected onto the plane perpendicular to the Higgs boson direction of flight.

One can obtain the polarization of the (anti)top quark by integrating Equation F.1 over the angle θ_{ℓ}^a (or θ_{ℓ}^b):

$$\frac{1}{\sigma} \frac{d\sigma}{d \cos \theta_{\ell^\pm}^a} = \frac{1}{2} \left(1 + \alpha_{\ell^\pm} P_{t,\bar{t}}^a \cos \theta_{\ell^\pm}^a \right), \quad (\text{F.4})$$

which applies to all the spin quantization axes used here.

It was also found that the energy distributions of the top quark decay products carry some information on the polarization state of the top (anti)quark [148–156]. We follow the same definitions used by [150, 152] and study the ratios of the different energies. We give the first two observables as follows

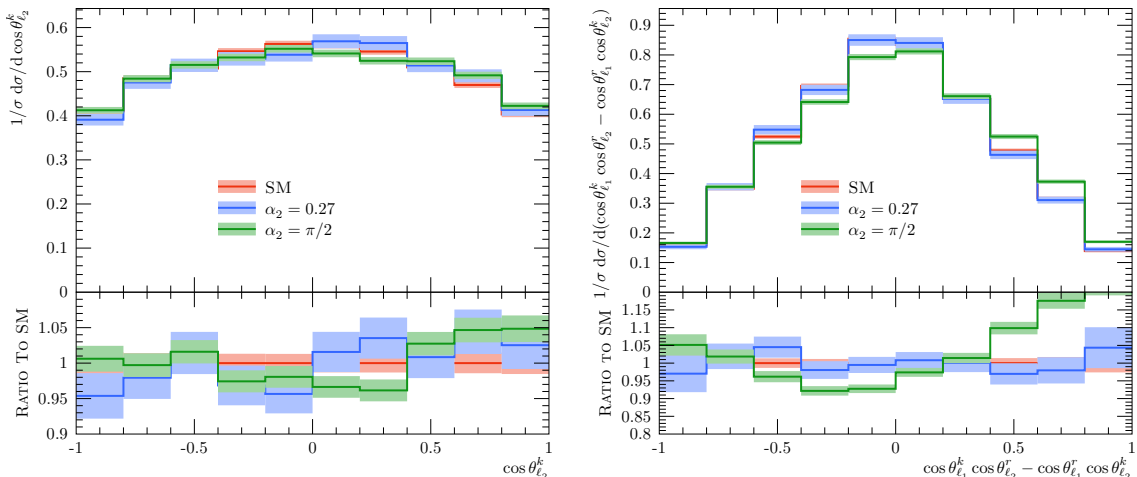
$$u = \frac{E_{\ell}}{E_{\ell} + E_b}, \quad z = \frac{E_b}{E_t}, \quad (\text{F.5})$$

where E_{ℓ} , E_b and E_t are the energies of the charged lepton, b -jet and top quark in the laboratory frame. Finally, we consider the energy of the charged leptons in the laboratory frame

$$x_{\ell} = \frac{2E_{\ell}}{m_t}, \quad (\text{F.6})$$

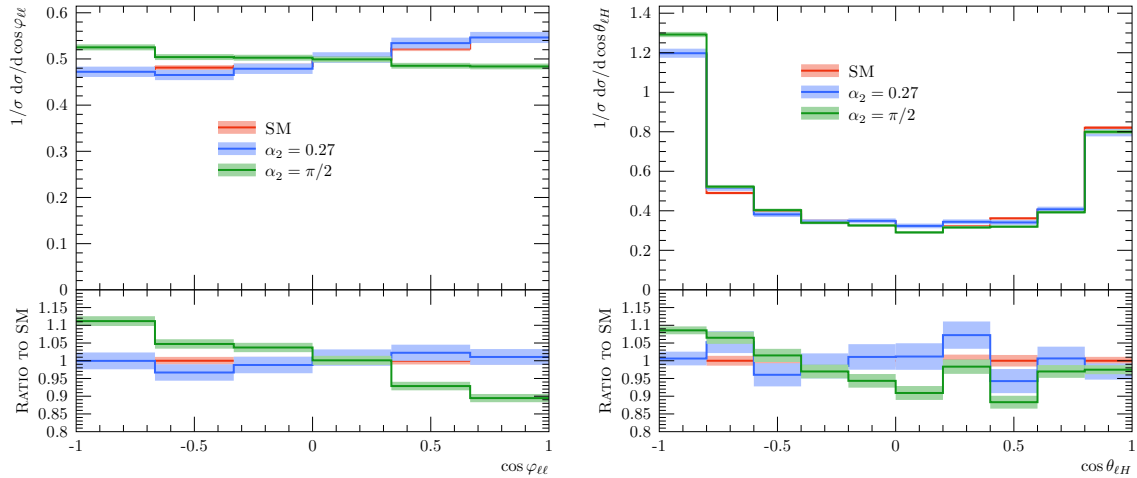
where $m_t = 172.5$ GeV is the pole mass of the top quark.

Figure 14. The double differential cross section in $\cos \theta_{\ell^n} \cos \theta_{\ell^n}$ in the transverse basis (left) and in $\cos \theta_{\ell^k} \cos \theta_{\ell^r} - \cos \theta_{\ell^r} \cos \theta_{\ell^k}$ in both the helicity and r -basis (right). Red lines are for the SM, blue lines are for the signal benchmark point with $\alpha_2 = 0.27$ while green lines are for the pure pseudoscalar case $\alpha_2 = \pi/2$ as a comparison, which is of course excluded.



In Figure 14, we show the $\cos \theta_{\ell_+}^k$ in the helicity basis (left panel) and an asymmetric

Figure 15. Left: Normalized distribution in the cosine of the opening angle between the two charged leptons ($\cos \varphi_{\ell_a \ell_b}$). Right: Normalized distribution in $\cos \theta_{\ell H}$ defined in Equation F.3.



combination of the same double-angle distribution in both the helicity and r -basis (right panel). The two figures show clearly significant sensitivity for $\alpha_2 = \pi/2$, while for $\alpha_2 = 0.27$ the sensitivity is rather mild. In Figure 15, we display the spectrum in the opening angle between the leptons from the fully leptonic decay of the $t\bar{t}$ system (left) and the $\cos \theta_{\ell H_1}$ distribution (right). The same conclusions as in the previous case apply for the case of $\alpha_2 = 0.27$ while differences of about 10% with respect to the SM case can be reached for $\alpha_2 = \pi/2$.

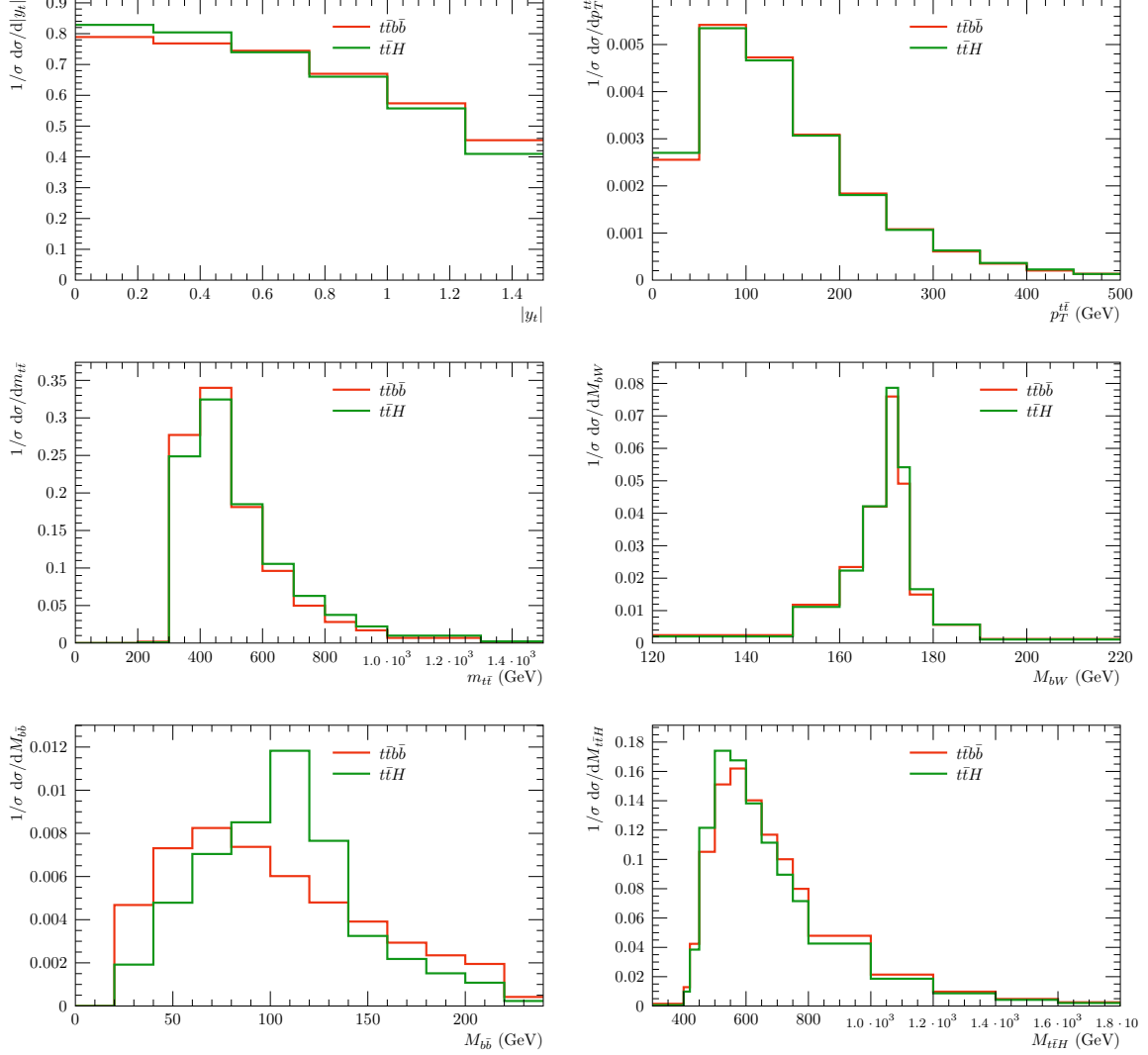
G Top Quark Reconstruction

For $t\bar{t}$ spin-spin correlation and polarization observables in the top quark rest frame, it is mandatory to fully reconstruct the top (anti)quark four-momentum. In this regard, we employ the PSEUDOTOP definition [157] widely used by the ATLAS and the CMS collaborations for, e.g., validation of MC event generators. We slightly modify the RIVET implementation of the CMS measurement of the $t\bar{t}$ differential cross section at $\sqrt{s} = 8$ TeV [158]. We minimize the following quantity

$$K^2 = (M_{\tilde{t}_\ell} - m_t)^2 + (M_{j_1 j_2} - m_W)^2 + (M_{\tilde{t}_h} - m_t)^2 + \left(M_{\tilde{p}_{H_1}} - m_{H_1} \right)^2, \quad (\text{G.1})$$

to select the hadronic, leptonic (anti)top quarks and SM-like Higgs boson decaying into $b\bar{b}$. In Equation G.1, m_t, m_W and m_H are the masses of the top quark, W boson and the Higgs boson, respectively, while $\tilde{t}_\ell(\tilde{t}_h)$ is the momentum of the (anti)top constructed in the leptonic(hadronic) decays of the W boson, with \tilde{p}_{H_1} the four-momentum of the Higgs boson candidate. In the reconstruction procedure, all jets and leptons in the event are considered provided they satisfy the selection criteria which was highlighted in subsection 5.1. Validation plots for the PSEUDOTOP reconstruction method in $t\bar{t}H_1(\rightarrow b\bar{b})$ (green) and the QCD-mediated $t\bar{t}b\bar{b}$ (red) are shown in Figure 16.

Figure 16. Validation plots for the PSEUDO-TOP reconstruction method in $t\bar{t}H_1(\rightarrow b\bar{b})$ (green) and the QCD-mediated $t\bar{t}b\bar{b}$ (red). Here, we show the absolute value of the rapidity of the top quark (upper left), the transverse momentum of the $t\bar{t}$ system (upper right), the invariant mass of the $t\bar{t}$ system (middle left), the one of the reconstructed top (anti)quark (middle right), the one of the Higgs boson (lower left) and the one of the $t\bar{t}H_1$ system (lower right).



References

- [1] J. H. Christenson, J. W. Cronin, V. L. Fitch and R. Turlay, *Evidence for the 2π Decay of the K_2^0 Meson*, *Phys. Rev. Lett.* **13** (1964) 138–140.
- [2] PARTICLE DATA GROUP collaboration, M. Tanabashi et al., *Review of Particle Physics*, *Phys. Rev.* **D98** (2018) 030001.
- [3] LHCb collaboration, R. Aaij et al., *Observation of CP Violation in Charm Decays*, *Phys. Rev. Lett.* **122** (2019) 211803, [[1903.08726](#)].
- [4] M. Kobayashi and T. Maskawa, *CP Violation in the Renormalizable Theory of Weak*

Interaction, *Prog. Theor. Phys.* **49** (1973) 652–657.

- [5] A. G. Cohen, D. B. Kaplan and A. E. Nelson, *Spontaneous baryogenesis at the weak phase transition*, *Phys. Lett.* **B263** (1991) 86–92.
- [6] A. G. Cohen, D. B. Kaplan and A. E. Nelson, *Progress in electroweak baryogenesis*, *Ann. Rev. Nucl. Part. Sci.* **43** (1993) 27–70, [[hep-ph/9302210](#)].
- [7] D. E. Morrissey and M. J. Ramsey-Musolf, *Electroweak baryogenesis*, *New J. Phys.* **14** (2012) 125003, [[1206.2942](#)].
- [8] J. Shu and Y. Zhang, *Impact of a CP Violating Higgs Sector: From LHC to Baryogenesis*, *Phys. Rev. Lett.* **111** (2013) 091801, [[1304.0773](#)].
- [9] I. B. Khriplovich and S. K. Lamoreaux, *CP violation without strangeness: Electric dipole moments of particles, atoms, and molecules*. 1997.
- [10] M. Pospelov and A. Ritz, *Electric dipole moments as probes of new physics*, *Annals Phys.* **318** (2005) 119–169, [[hep-ph/0504231](#)].
- [11] J. Engel, M. J. Ramsey-Musolf and U. van Kolck, *Electric Dipole Moments of Nucleons, Nuclei, and Atoms: The Standard Model and Beyond*, *Prog. Part. Nucl. Phys.* **71** (2013) 21–74, [[1303.2371](#)].
- [12] M. S. Safronova, D. Budker, D. DeMille, D. F. J. Kimball, A. Derevianko and C. W. Clark, *Search for New Physics with Atoms and Molecules*, *Rev. Mod. Phys.* **90** (2018) 025008, [[1710.01833](#)].
- [13] T. Chupp, P. Fierlinger, M. Ramsey-Musolf and J. Singh, *Electric dipole moments of atoms, molecules, nuclei, and particles*, *Rev. Mod. Phys.* **91** (2019) 015001, [[1710.02504](#)].
- [14] ACME collaboration, V. Andreev et al., *Improved limit on the electric dipole moment of the electron*, *Nature* **562** (2018) 355–360.
- [15] C. A. Baker et al., *An Improved experimental limit on the electric dipole moment of the neutron*, *Phys. Rev. Lett.* **97** (2006) 131801, [[hep-ex/0602020](#)].
- [16] J. M. Pendlebury et al., *Revised experimental upper limit on the electric dipole moment of the neutron*, *Phys. Rev.* **D92** (2015) 092003, [[1509.04411](#)].
- [17] nEDM collaboration, C. Abel et al., *Measurement of the permanent electric dipole moment of the neutron*, *Phys. Rev. Lett.* **124** (2020) 081803, [[2001.11966](#)].
- [18] HL/HE WG2 GROUP collaboration, M. Cepeda et al., *Higgs Physics at the HL-LHC and HE-LHC*, [1902.00134](#).
- [19] C. R. Schmidt and M. E. Peskin, *A Probe of CP violation in top quark pair production at hadron supercolliders*, *Phys. Rev. Lett.* **69** (1992) 410–413.
- [20] G. Mahlon and S. J. Parke, *Angular correlations in top quark pair production and decay at hadron colliders*, *Phys. Rev.* **D53** (1996) 4886–4896, [[hep-ph/9512264](#)].
- [21] F. Boudjema, R. M. Godbole, D. Guadagnoli and K. A. Mohan, *Lab-frame observables for probing the top-Higgs interaction*, *Phys. Rev.* **D92** (2015) 015019, [[1501.03157](#)].
- [22] M. R. Buckley and D. Goncalves, *Boosting the Direct CP Measurement of the Higgs-Top Coupling*, *Phys. Rev. Lett.* **116** (2016) 091801, [[1507.07926](#)].
- [23] S. Amor Dos Santos et al., *Probing the CP nature of the Higgs coupling in $t\bar{t}h$ events at the LHC*, *Phys. Rev.* **D96** (2017) 013004, [[1704.03565](#)].

- [24] D. Azevedo, A. Onofre, F. Filthaut and R. Goncalo, *CP tests of Higgs couplings in $t\bar{t}h$ semileptonic events at the LHC*, *Phys. Rev.* **D98** (2018) 033004, [[1711.05292](#)].
- [25] P. S. Bhupal Dev, A. Djouadi, R. M. Godbole, M. M. Muhlleitner and S. D. Rindani, *Determining the CP properties of the Higgs boson*, *Phys. Rev. Lett.* **100** (2008) 051801, [[0707.2878](#)].
- [26] W. Bernreuther, L. Chen, I. García, M. Perelló, R. Poeschl, F. Richard et al., *CP-violating top quark couplings at future linear e^+e^- colliders*, *Eur. Phys. J.* **C78** (2018) 155, [[1710.06737](#)].
- [27] K. Hagiwara, H. Yokoya and Y.-J. Zheng, *Probing the CP properties of top Yukawa coupling at an e^+e^- collider*, *JHEP* **02** (2018) 180, [[1712.09953](#)].
- [28] K. Desch, A. Imhof, Z. Was and M. Worek, *Probing the CP nature of the Higgs boson at linear colliders with tau spin correlations: The Case of mixed scalar - pseudoscalar couplings*, *Phys. Lett.* **B579** (2004) 157–164, [[hep-ph/0307331](#)].
- [29] S. Berge, W. Bernreuther and J. Ziethe, *Determining the CP parity of Higgs bosons at the LHC in their tau decay channels*, *Phys. Rev. Lett.* **100** (2008) 171605, [[0801.2297](#)].
- [30] R. Harnik, A. Martin, T. Okui, R. Primulando and F. Yu, *Measuring CP Violation in $h \rightarrow \tau^+\tau^-$ at Colliders*, *Phys. Rev.* **D88** (2013) 076009, [[1308.1094](#)].
- [31] S. Berge, W. Bernreuther and H. Spiesberger, *Higgs CP properties using the τ decay modes at the ILC*, *Phys. Lett.* **B727** (2013) 488–495, [[1308.2674](#)].
- [32] S. Berge, W. Bernreuther and S. Kirchner, *Prospects of constraining the Higgs boson’s CP nature in the tau decay channel at the LHC*, *Phys. Rev.* **D92** (2015) 096012, [[1510.03850](#)].
- [33] A. Askew, P. Jaiswal, T. Okui, H. B. Prosper and N. Sato, *Prospect for measuring the CP phase in the $h\tau\tau$ coupling at the LHC*, *Phys. Rev.* **D91** (2015) 075014, [[1501.03156](#)].
- [34] R. Józefowicz, E. Richter-Was and Z. Was, *Potential for optimizing the Higgs boson CP measurement in $H \rightarrow \tau\tau$ decays at the LHC including machine learning techniques*, *Phys. Rev.* **D94** (2016) 093001, [[1608.02609](#)].
- [35] ATLAS collaboration, G. Aad et al., *Observation of a new particle in the search for the Standard Model Higgs boson with the ATLAS detector at the LHC*, *Phys. Lett.* **B716** (2012) 1–29, [[1207.7214](#)].
- [36] CMS collaboration, S. Chatrchyan et al., *Observation of a New Boson at a Mass of 125 GeV with the CMS Experiment at the LHC*, *Phys. Lett.* **B716** (2012) 30–61, [[1207.7235](#)].
- [37] ATLAS, CMS collaboration, G. Aad et al., *Combined Measurement of the Higgs Boson Mass in pp Collisions at $\sqrt{s} = 7$ and 8 TeV with the ATLAS and CMS Experiments*, *Phys. Rev. Lett.* **114** (2015) 191803, [[1503.07589](#)].
- [38] G. Li, Y.-n. Mao, C. Zhang and S.-h. Zhu, *Testing CP violation in the scalar sector at future e^+e^- colliders*, *Phys. Rev.* **D95** (2017) 035015, [[1611.08518](#)].
- [39] Y.-n. Mao, *Spontaneous CP-violation in the Simplest Little Higgs Model and its Future Collider Tests: the Scalar Sector*, *Phys. Rev.* **D97** (2018) 075031, [[1703.10123](#)].
- [40] Y.-n. Mao, *Spontaneous CP-violation in the Simplest Little Higgs Model*, *PoS ICHEP2018* (2019) 003, [[1810.03854](#)].
- [41] L. Bento, G. C. Branco and P. A. Parada, *A Minimal model with natural suppression of strong CP violation*, *Phys. Lett.* **B267** (1991) 95–99.

- [42] T. D. Lee, *A Theory of Spontaneous T Violation*, *Phys. Rev.* **D8** (1973) 1226–1239.
- [43] T. D. Lee, *CP Nonconservation and Spontaneous Symmetry Breaking*, *Phys. Rept.* **9** (1974) 143–177.
- [44] H. Georgi, *A Model of Soft CP Violation*, *Hadronic J.* **1** (1978) 155.
- [45] G. C. Branco, P. M. Ferreira, L. Lavoura, M. N. Rebelo, M. Sher and J. P. Silva, *Theory and phenomenology of two-Higgs-doublet models*, *Phys. Rept.* **516** (2012) 1–102, [[1106.0034](#)].
- [46] S. Weinberg, *Gauge Theory of CP Violation*, *Phys. Rev. Lett.* **37** (1976) 657.
- [47] A. W. El Kaffas, W. Khater, O. M. Ogreid and P. Osland, *Consistency of the two Higgs doublet model and CP violation in top production at the LHC*, *Nucl. Phys.* **B775** (2007) 45–77, [[hep-ph/0605142](#)].
- [48] P. Osland, P. N. Pandita and L. Selbuz, *Trilinear Higgs couplings in the two Higgs doublet model with CP violation*, *Phys. Rev.* **D78** (2008) 015003, [[0802.0060](#)].
- [49] A. Arhrib, E. Christova, H. Eberl and E. Ginina, *CP violation in charged Higgs production and decays in the Complex Two Higgs Doublet Model*, *JHEP* **04** (2011) 089, [[1011.6560](#)].
- [50] BELLE collaboration, A. Abdesselam et al., *Measurement of the inclusive $B \rightarrow X_{s+d}\gamma$ branching fraction, photon energy spectrum and HQE parameters*, in *Proceedings, 38th International Conference on High Energy Physics (ICHEP 2016): Chicago, IL, USA, August 3-10, 2016*, 2016, [1608.02344](#).
- [51] M. Misiak and M. Steinhauser, *Weak radiative decays of the B meson and bounds on M_{H^\pm} in the Two-Higgs-Doublet Model*, *Eur. Phys. J.* **C77** (2017) 201, [[1702.04571](#)].
- [52] M. E. Peskin and T. Takeuchi, *A New constraint on a strongly interacting Higgs sector*, *Phys. Rev. Lett.* **65** (1990) 964–967.
- [53] M. E. Peskin and T. Takeuchi, *Estimation of oblique electroweak corrections*, *Phys. Rev.* **D46** (1992) 381–409.
- [54] J. de Blas, M. Ciuchini, E. Franco, S. Mishima, M. Pierini, L. Reina et al., *Electroweak precision observables and Higgs-boson signal strengths in the Standard Model and beyond: present and future*, *JHEP* **12** (2016) 135, [[1608.01509](#)].
- [55] W. Grimus, L. Lavoura, O. M. Ogreid and P. Osland, *A Precision constraint on multi-Higgs-doublet models*, *J. Phys.* **G35** (2008) 075001, [[0711.4022](#)].
- [56] W. Grimus, L. Lavoura, O. M. Ogreid and P. Osland, *The Oblique parameters in multi-Higgs-doublet models*, *Nucl. Phys.* **B801** (2008) 81–96, [[0802.4353](#)].
- [57] H. E. Haber and D. O’Neil, *Basis-independent methods for the two-Higgs-doublet model III: The CP-conserving limit, custodial symmetry, and the oblique parameters S, T, U*, *Phys. Rev.* **D83** (2011) 055017, [[1011.6188](#)].
- [58] D. Egana-Ugrinovic and S. Thomas, *Higgs Boson Contributions to the Electron Electric Dipole Moment*, [1810.08631](#).
- [59] Y.-n. Mao and S.-h. Zhu, *Lightness of Higgs boson and spontaneous CP violation in the Lee model*, *Phys. Rev.* **D90** (2014) 115024, [[1409.6844](#)].
- [60] L. Bian, T. Liu and J. Shu, *Cancellations Between Two-Loop Contributions to the Electron Electric Dipole Moment with a CP-Violating Higgs Sector*, *Phys. Rev. Lett.* **115** (2015) 021801, [[1411.6695](#)].

- [61] Y.-n. Mao and S.-h. Zhu, *Lightness of a Higgs Boson and Spontaneous CP-violation in the Lee Model: An Alternative Scenario*, *Phys. Rev.* **D94** (2016) 055008, [[1602.00209](#)].
- [62] L. Bian and N. Chen, *Higgs pair productions in the CP-violating two-Higgs-doublet model*, *JHEP* **09** (2016) 069, [[1607.02703](#)].
- [63] L. Bian and N. Chen, *Cancellation mechanism in the predictions of electric dipole moments*, *Phys. Rev.* **D95** (2017) 115029, [[1608.07975](#)].
- [64] K. Fuyuto, W.-S. Hou and E. Senaha, *Cancellation mechanism for the electron electric dipole moment connected with baryon asymmetry of the Universe*, [1910.12404](#).
- [65] T. Chupp and M. Ramsey-Musolf, *Electric Dipole Moments: A Global Analysis*, *Phys. Rev.* **C91** (2015) 035502, [[1407.1064](#)].
- [66] C. Cesarotti, Q. Lu, Y. Nakai, A. Parikh and M. Reece, *Interpreting the Electron EDM Constraint*, *JHEP* **05** (2019) 059, [[1810.07736](#)].
- [67] N. Yamanaka, *Analysis of the Electric Dipole Moment in the R-parity Violating Supersymmetric Standard Model*, Ph.D. thesis, Osaka U., Res. Ctr. Nucl. Phys., 2013. 10.1007/978-4-431-54544-6.
- [68] S. M. Barr and A. Zee, *Electric Dipole Moment of the Electron and of the Neutron*, *Phys. Rev. Lett.* **65** (1990) 21–24.
- [69] D. Chang, W.-Y. Keung and T. C. Yuan, *Two loop bosonic contribution to the electron electric dipole moment*, *Phys. Rev.* **D43** (1991) R14–R16.
- [70] R. G. Leigh, S. Paban and R. M. Xu, *Electric dipole moment of electron*, *Nucl. Phys.* **B352** (1991) 45–58.
- [71] T. Abe, J. Hisano, T. Kitahara and K. Tobioka, *Gauge invariant Barr-Zee type contributions to fermionic EDMs in the two-Higgs doublet models*, *JHEP* **01** (2014) 106, [[1311.4704](#)].
- [72] J. Brod, U. Haisch and J. Zupan, *Constraints on CP-violating Higgs couplings to the third generation*, *JHEP* **11** (2013) 180, [[1310.1385](#)].
- [73] K. Cheung, J. S. Lee, E. Senaha and P.-Y. Tseng, *Confronting Higgscision with Electric Dipole Moments*, *JHEP* **06** (2014) 149, [[1403.4775](#)].
- [74] W. Altmannshofer, J. Brod and M. Schmaltz, *Experimental constraints on the coupling of the Higgs boson to electrons*, *JHEP* **05** (2015) 125, [[1503.04830](#)].
- [75] S. M. Barr, *Measurable T and P odd electron - nucleon interactions from Higgs boson exchange*, *Phys. Rev. Lett.* **68** (1992) 1822–1825.
- [76] W. Dekens, J. de Vries, M. Jung and K. K. Vos, *The phenomenology of electric dipole moments in models of scalar leptoquarks*, *JHEP* **01** (2019) 069, [[1809.09114](#)].
- [77] K. Cheung, W.-Y. Keung, Y.-n. Mao and C. Zhang, *Constraining CP-violating electron-gluonic operators*, *JHEP* **07** (2019) 074, [[1904.10808](#)].
- [78] H.-Y. Cheng and C.-W. Chiang, *Revisiting Scalar and Pseudoscalar Couplings with Nucleons*, *JHEP* **07** (2012) 009, [[1202.1292](#)].
- [79] R. J. Hill and M. P. Solon, *Standard Model anatomy of WIMP dark matter direct detection II: QCD analysis and hadronic matrix elements*, *Phys. Rev.* **D91** (2015) 043505, [[1409.8290](#)].

- [80] xQCD collaboration, Y.-B. Yang, A. Alexandru, T. Draper, J. Liang and K.-F. Liu, πN and strangeness sigma terms at the physical point with chiral fermions, *Phys. Rev.* **D94** (2016) 054503, [[1511.09089](#)].
- [81] X.-D. Ji, *A QCD analysis of the mass structure of the nucleon*, *Phys. Rev. Lett.* **74** (1995) 1071–1074, [[hep-ph/9410274](#)].
- [82] S. Weinberg, *Larger Higgs Exchange Terms in the Neutron Electric Dipole Moment*, *Phys. Rev. Lett.* **63** (1989) 2333.
- [83] D. A. Dicus, *Neutron Electric Dipole Moment From Charged Higgs Exchange*, *Phys. Rev.* **D41** (1990) 999.
- [84] E. Braaten, C.-S. Li and T.-C. Yuan, *The Evolution of Weinberg’s Gluonic CP Violation Operator*, *Phys. Rev. Lett.* **64** (1990) 1709.
- [85] G. Degrossi, E. Franco, S. Marchetti and L. Silvestrini, *QCD corrections to the electric dipole moment of the neutron in the MSSM*, *JHEP* **11** (2005) 044, [[hep-ph/0510137](#)].
- [86] S. Aoki et al., *Review of lattice results concerning low-energy particle physics*, *Eur. Phys. J.* **C77** (2017) 112, [[1607.00299](#)].
- [87] FLAVOUR LATTICE AVERAGING GROUP collaboration, S. Aoki et al., *FLAG Review 2019*, [1902.08191](#).
- [88] J. Hisano, J. Y. Lee, N. Nagata and Y. Shimizu, *Reevaluation of Neutron Electric Dipole Moment with QCD Sum Rules*, *Phys. Rev.* **D85** (2012) 114044, [[1204.2653](#)].
- [89] D. A. Demir, M. Pospelov and A. Ritz, *Hadronic EDMs, the Weinberg operator, and light gluinos*, *Phys. Rev.* **D67** (2003) 015007, [[hep-ph/0208257](#)].
- [90] C. McNeile, A. Bazavov, C. T. H. Davies, R. J. Dowdall, K. Hornbostel, G. P. Lepage et al., *Direct determination of the strange and light quark condensates from full lattice QCD*, *Phys. Rev.* **D87** (2013) 034503, [[1211.6577](#)].
- [91] C. A. Baker et al., *CryoEDM: A cryogenic experiment to measure the neutron electric dipole moment*, *J. Phys. Conf. Ser.* **251** (2010) 012055.
- [92] R. Picker, *How the minuscule can contribute to the big picture: the neutron electric dipole moment project at TRIUMF*, *JPS Conf. Proc.* **13** (2017) 010005, [[1612.00875](#)].
- [93] N. Ayres, *Data and Systematic Error Analysis for the Neutron Electric Dipole Moment Experiment at the Paul Scherrer Institute and Search for Axionlike Dark Matter*, Ph.D. thesis, Sussex U., 2018-12-14.
- [94] C. Abel et al., *The n2EDM experiment at the Paul Scherrer Institute*, in *International Workshop on Particle Physics at Neutron Sources 2018 (PPNS 2018) Grenoble, France, May 24-26, 2018*, 2018, [1811.02340](#).
- [95] LHC Higgs Cross Section Working Group, S. Dittmaier, C. Mariotti, G. Passarino and R. Tanaka (Eds.), *Handbook of LHC Higgs Cross Sections: 1. Inclusive Observables*, *CERN-2011-002* (CERN, Geneva, 2011) , [[1101.0593](#)].
- [96] S. Dittmaier et al., *Handbook of LHC Higgs Cross Sections: 2. Differential Distributions*, [1201.3084](#).
- [97] LHC HIGGS CROSS SECTION WORKING GROUP collaboration, J. R. Andersen et al., *Handbook of LHC Higgs Cross Sections: 3. Higgs Properties*, [1307.1347](#).

- [98] LHC HIGGS CROSS SECTION WORKING GROUP collaboration, D. de Florian et al., *Handbook of LHC Higgs Cross Sections: 4. Deciphering the Nature of the Higgs Sector*, [1610.07922](#).
- [99] ATLAS collaboration, G. Aad et al., *Combined measurements of Higgs boson production and decay using up to 80 fb⁻¹ of proton-proton collision data at $\sqrt{s} = 13$ TeV collected with the ATLAS experiment*, *Phys. Rev.* **D101** (2020) 012002, [[1909.02845](#)].
- [100] ATLAS, CMS collaboration, L. Cadamuro, *Higgs boson couplings and properties*, *PoS LHCP2019* (2019) 101.
- [101] ATLAS collaboration, *Measurement of Higgs boson production in association with a $t\bar{t}$ pair in the diphoton decay channel using 139 fb⁻¹ of LHC data collected at $\sqrt{s} = 13$ TeV by the ATLAS experiment*, Tech. Rep. ATLAS-CONF-2019-004, CERN, Geneva, Mar, 2019.
- [102] ATLAS collaboration, M. Aaboud et al., *Observation of Higgs boson production in association with a top quark pair at the LHC with the ATLAS detector*, *Phys. Lett.* **B784** (2018) 173–191, [[1806.00425](#)].
- [103] CMS collaboration, *Combined Higgs boson production and decay measurements with up to 137 fb⁻¹ of proton-proton collision data at $\sqrt{s} = 13$ TeV*, Tech. Rep. CMS-PAS-HIG-19-005, CERN, Geneva, 2020.
- [104] CMS collaboration, A. M. Sirunyan et al., *Combined measurements of Higgs boson couplings in proton-proton collisions at $\sqrt{s} = 13$ TeV*, *Eur. Phys. J.* **C79** (2019) 421, [[1809.10733](#)].
- [105] CMS collaboration, A. M. Sirunyan et al., *Observation of Higgs boson decay to bottom quarks*, *Phys. Rev. Lett.* **121** (2018) 121801, [[1808.08242](#)].
- [106] A. Djouadi, *The Anatomy of electro-weak symmetry breaking. I: The Higgs boson in the standard model*, *Phys. Rept.* **457** (2008) 1–216, [[hep-ph/0503172](#)].
- [107] A. Djouadi, *The Anatomy of electro-weak symmetry breaking. II. The Higgs bosons in the minimal supersymmetric model*, *Phys. Rept.* **459** (2008) 1–241, [[hep-ph/0503173](#)].
- [108] H.-L. Li, P.-C. Lu, Z.-G. Si and Y. Wang, *Associated Production of Higgs Boson and $t\bar{t}$ at LHC*, *Chin. Phys.* **C40** (2016) 063102, [[1508.06416](#)].
- [109] ATLAS collaboration, *Search for heavy ZZ resonances in the $\ell^+\ell^-\ell^+\ell^-$ and $\ell^+\ell^-\nu\bar{\nu}$ final states using proton-proton collisions at $\sqrt{s} = 13$ TeV with the ATLAS detector*, Tech. Rep. ATLAS-CONF-2017-058, CERN, Geneva, Jul, 2017.
- [110] A. D. Martin, W. J. Stirling, R. S. Thorne and G. Watt, *Parton distributions for the LHC*, *Eur. Phys. J.* **C63** (2009) 189–285, [[0901.0002](#)].
- [111] ATLAS collaboration, M. Aaboud et al., *Search for heavy particles decaying into top-quark pairs using lepton-plus-jets events in proton-proton collisions at $\sqrt{s} = 13$ TeV with the ATLAS detector*, *Eur. Phys. J.* **C78** (2018) 565, [[1804.10823](#)].
- [112] D. Dicus, A. Stange and S. Willenbrock, *Higgs decay to top quarks at hadron colliders*, *Phys. Lett.* **B333** (1994) 126–131, [[hep-ph/9404359](#)].
- [113] A. Djouadi, J. Ellis, A. Popov and J. Quevillon, *Interference effects in $t\bar{t}$ production at the LHC as a window on new physics*, *JHEP* **03** (2019) 119, [[1901.03417](#)].
- [114] ATLAS collaboration, M. Aaboud et al., *Search for Heavy Higgs Bosons A/H Decaying to a Top Quark Pair in pp Collisions at $\sqrt{s} = 8$ TeV with the ATLAS Detector*, *Phys. Rev. Lett.* **119** (2017) 191803, [[1707.06025](#)].

- [115] CMS collaboration, A. M. Sirunyan et al., *Search for heavy Higgs bosons decaying to a top quark pair in proton-proton collisions at $\sqrt{s} = 13$ TeV*, [1908.01115](#).
- [116] CMS collaboration, *Search for standard model production of four top quarks in final states with same-sign and multiple leptons in proton-proton collisions at $\sqrt{s} = 13$ TeV*, Tech. Rep. CMS-PAS-TOP-18-003, CERN, Geneva, 2019.
- [117] Q.-H. Cao, S.-L. Chen, Y. Liu, R. Zhang and Y. Zhang, *Limiting top quark-Higgs boson interaction and Higgs-boson width from multitop productions*, *Phys. Rev.* **D99** (2019) [113003](#), [[1901.04567](#)].
- [118] J. Alwall, M. Herquet, F. Maltoni, O. Mattelaer and T. Stelzer, *MadGraph 5 : Going Beyond*, *JHEP* **06** (2011) [128](#), [[1106.0522](#)].
- [119] J. Alwall, R. Frederix, S. Frixione, V. Hirschi, F. Maltoni, O. Mattelaer et al., *The automated computation of tree-level and next-to-leading order differential cross sections, and their matching to parton shower simulations*, *JHEP* **07** (2014) [079](#), [[1405.0301](#)].
- [120] CMS collaboration, A. M. Sirunyan et al., *Search for a charged Higgs boson decaying into top and bottom quarks in events with electrons or muons in proton-proton collisions at $\sqrt{s} = 13$ TeV*, *JHEP* **01** (2020) [096](#), [[1908.09206](#)].
- [121] CMS collaboration, *Search for charged Higgs bosons decaying into top and a bottom quark in the fully hadronic final state at 13 TeV*, Tech. Rep. CMS-PAS-HIG-18-015, CERN, Geneva, 2019.
- [122] A. Arhrib, D. Azevedo, R. Benbrik, H. Harouiz, S. Moretti, R. Patrick et al., *Signal versus Background Interference in $H^+ \rightarrow t\bar{b}$ Signals for MSSM Benchmark Scenarios*, [1905.02635](#).
- [123] C. Degrande, C. Duhr, B. Fuks, D. Grellscheid, O. Mattelaer and T. Reiter, *UFO - The Universal FeynRules Output*, *Comput. Phys. Commun.* **183** (2012) [1201–1214](#), [[1108.2040](#)].
- [124] C. Degrande, *Automatic evaluation of UV and R2 terms for beyond the Standard Model Lagrangians: a proof-of-principle*, *Comput. Phys. Commun.* **197** (2015) [239–262](#), [[1406.3030](#)].
- [125] L. A. Harland-Lang, A. D. Martin, P. Motylinski and R. S. Thorne, *Parton distributions in the LHC era: MMHT 2014 PDFs*, *Eur. Phys. J.* **C75** (2015) [204](#), [[1412.3989](#)].
- [126] A. Kalogeropoulos and J. Alwall, *The SysCalc code: A tool to derive theoretical systematic uncertainties*, [1801.08401](#).
- [127] P. Artoisenet, R. Frederix, O. Mattelaer and R. Rietkerk, *Automatic spin-entangled decays of heavy resonances in Monte Carlo simulations*, *JHEP* **03** (2013) [015](#), [[1212.3460](#)].
- [128] T. Sjöstrand, S. Ask, J. R. Christiansen, R. Corke, N. Desai, P. Ilten et al., *An Introduction to PYTHIA 8.2*, *Comput. Phys. Commun.* **191** (2015) [159–177](#), [[1410.3012](#)].
- [129] M. Dobbs and J. B. Hansen, *The HepMC C++ Monte Carlo event record for High Energy Physics*, *Comput. Phys. Commun.* **134** (2001) [41–46](#).
- [130] A. Buckley, J. Butterworth, L. Lönnblad, D. Grellscheid, H. Hoeth, J. Monk et al., *Rivet user manual*, *Comput. Phys. Commun.* **184** (2013) [2803–2819](#), [[1003.0694](#)].
- [131] M. Cacciari, G. P. Salam and G. Soyez, *The Anti- $k(t)$ jet clustering algorithm*, *JHEP* **04** (2008) [063](#), [[0802.1189](#)].
- [132] M. Cacciari, G. P. Salam and G. Soyez, *FastJet User Manual*, *Eur. Phys. J.* **C72** (2012) [1896](#), [[1111.6097](#)].

- [133] G. Corcella, I. G. Knowles, G. Marchesini, S. Moretti, K. Odagiri, P. Richardson et al., *HERWIG 6.5 release note*, [hep-ph/0210213](#).
- [134] G. Corcella, I. G. Knowles, G. Marchesini, S. Moretti, K. Odagiri, P. Richardson et al., *HERWIG 6.4 release note*, [hep-ph/0201201](#).
- [135] G. Corcella, I. G. Knowles, G. Marchesini, S. Moretti, K. Odagiri, P. Richardson et al., *HERWIG 6.3 release note*, [hep-ph/0107071](#).
- [136] G. Corcella, I. G. Knowles, G. Marchesini, S. Moretti, K. Odagiri, P. Richardson et al., *HERWIG 6: An Event generator for hadron emission reactions with interfering gluons (including supersymmetric processes)*, *JHEP* **01** (2001) 010, [[hep-ph/0011363](#)].
- [137] M. Wobisch and T. Wengler, *Hadronization corrections to jet cross-sections in deep inelastic scattering*, in *Monte Carlo generators for HERA physics. Proceedings, Workshop, Hamburg, Germany, 1998-1999*, pp. 270–279, 1998, [hep-ph/9907280](#).
- [138] Y. L. Dokshitzer, G. D. Leder, S. Moretti and B. R. Webber, *Better jet clustering algorithms*, *JHEP* **08** (1997) 001, [[hep-ph/9707323](#)].
- [139] M. Cacciari and G. P. Salam, *Pileup subtraction using jet areas*, *Phys. Lett.* **B659** (2008) 119–126, [[0707.1378](#)].
- [140] M. Cacciari, G. P. Salam and G. Soyez, *The Catchment Area of Jets*, *JHEP* **04** (2008) 005, [[0802.1188](#)].
- [141] J. Pumplin, D. Stump, R. Brock, D. Casey, J. Huston, J. Kalk et al., *Uncertainties of predictions from parton distribution functions. 2. The Hessian method*, *Phys. Rev.* **D65** (2001) 014013, [[hep-ph/0101032](#)].
- [142] S. D. Rindani, P. Sharma and A. W. Thomas, *Polarization of top quark as a probe of its chromomagnetic and chromoelectric couplings in tW production at the Large Hadron Collider*, *JHEP* **10** (2015) 180, [[1507.08385](#)].
- [143] W. Bernreuther and Z.-G. Si, *Top quark spin correlations and polarization at the LHC: standard model predictions and effects of anomalous top chromo moments*, *Phys. Lett.* **B725** (2013) 115–122, [[1305.2066](#)].
- [144] ATLAS collaboration, M. Aaboud et al., *Measurements of top quark spin observables in $t\bar{t}$ events using dilepton final states in $\sqrt{s} = 8$ TeV pp collisions with the ATLAS detector*, *JHEP* **03** (2017) 113, [[1612.07004](#)].
- [145] CMS collaboration, A. M. Sirunyan et al., *Measurement of the top quark polarization and $t\bar{t}$ spin correlations using dilepton final states in proton-proton collisions at $\sqrt{s} = 13$ TeV*, *Phys. Rev.* **D100** (2019) 072002, [[1907.03729](#)].
- [146] ATLAS collaboration, *Measurements of top-quark pair spin correlations in the $e\mu$ channel at $\sqrt{s} = 13$ TeV using pp collisions in the ATLAS detector*, Tech. Rep. ATLAS-CONF-2018-027, CERN, Geneva, Jul, 2018.
- [147] CMS collaboration, *Measurements of differential cross sections for $t\bar{t}$ production in proton-proton collisions at $\sqrt{s} = 13$ TeV using events containing two leptons*, Tech. Rep. CMS-PAS-TOP-17-014, CERN, Geneva, 2018.
- [148] R. M. Godbole, L. Hartgring, I. Niessen and C. D. White, *Top polarisation studies in H^-t and Wt production*, *JHEP* **01** (2012) 011, [[1111.0759](#)].

- [149] S. D. Rindani and P. Sharma, *Probing anomalous tbW couplings in single-top production using top polarization at the Large Hadron Collider*, *JHEP* **11** (2011) 082, [[1107.2597](#)].
- [150] A. Prasath V, R. M. Godbole and S. D. Rindani, *Longitudinal top polarisation measurement and anomalous Wtb coupling*, *Eur. Phys. J.* **C75** (2015) 402, [[1405.1264](#)].
- [151] R. M. Godbole, G. Mendiratta and S. Rindani, *Looking for bSM physics using top-quark polarization and decay-lepton kinematic asymmetries*, *Phys. Rev.* **D92** (2015) 094013, [[1506.07486](#)].
- [152] A. Jueid, *Probing anomalous Wtb couplings at the LHC in single t -channel top quark production*, *Phys. Rev.* **D98** (2018) 053006, [[1805.07763](#)].
- [153] A. Arhrib, A. Jueid and S. Moretti, *Top quark polarization as a probe of charged Higgs bosons*, *Phys. Rev.* **D98** (2018) 115006, [[1807.11306](#)].
- [154] R. Godbole, M. Guchait, C. K. Khosa, J. Lahiri, S. Sharma and A. H. Vijay, *Boosted Top quark polarization*, *Phys. Rev.* **D100** (2019) 056010, [[1902.08096](#)].
- [155] A. Arhrib, A. Jueid and S. Moretti, *Searching for Heavy Charged Higgs Bosons through Top Quark Polarization*, [1903.11489](#).
- [156] S. Chatterjee, R. Godbole and T. S. Roy, *Jets with electrons from boosted top quarks*, *JHEP* **01** (2020) 170, [[1909.11041](#)].
- [157] CMS collaboration, *Object definitions for top quark analyses at the particle level*, Tech. Rep. CMS-NOTE-2017-004, CERN-CMS-NOTE-2017-004, CERN, Geneva, Jun, 2017.
- [158] CMS collaboration, V. Khachatryan et al., *Measurement of the differential cross section for top quark pair production in pp collisions at $\sqrt{s} = 8$ TeV*, *Eur. Phys. J.* **C75** (2015) 542, [[1505.04480](#)].